AIMS Mathematics, 10(6): 14560–14595.
DOI: 10.3934/math.2025656
Received: 27 January 2025
Revised: 12 May 2025
Accepted: 21 May 2025
Published: 26 June 2025

https://www.aimspress.com/journal/Math

Research article

A mathematical and numerical study of an age-dependent transactivation model for dynamics of HIV infection

Luis X. Vivas-Cruz[1], **Celia Martínez-Lázaro**[1] **and Cruz Vargas-De-León**[2,3,*]

[1] Facultad de Matemáticas, Posgrado en Matemáticas, Universidad Autónoma de Guerrero, Av. Lázaro Cárdenas, Cd. Universitaria Sur, Chilpancingo, Guerrero, México

[2] División de Investigación, Hospital Juárez de México, Ciudad de México 07760, Mexico

[3] Laboratorio de Modelación Bioestadística para la Salud, Sección de Estudios de Posgrado e Investigación, Escuela Superior de Medicina, Instituto Politécnico Nacional, Ciudad de México 11340, Mexico

* **Correspondence:** Email: leoncruz82@yahoo.com.mx.

Abstract: We analyze a mathematical model for the dynamics of HIV infection that incorporates an age-dependent transactivation rate and reversion into latency. The basic reproduction number R_0 for viral infection has been determined, and it completely characterizes the global behavior of model solutions: If $R_0 > 1$, the infection is chronic, and if $R_0 \leq 1$, the infection is cleared. By constructing suitable Volterra-type Lyapunov functionals, it has been demonstrated that the corresponding equilibrium is globally stable in each of the two settings for R_0. We used the gamma distribution to define the age-dependent transactivation rate, which is the ratio of the probability density function to the complement of the cumulative distribution function. We present some numerical simulations in each of the two settings for the R_0 of the age-structured model, where the subsystem of ODE was solved by the fourth-order Runge–Kutta method and the hyperbolic partial differential equation (PDE) is solved by the Crank–Nicolson method, which is second-order in time and age. In conclusion, we have provided the complete classification for the global dynamics of the age-structured model. Possible strategies to control a viral infection have been identified through sensitivity analysis.

Keywords: infection age; fourth-order Runge–Kutta method; Crank–Nicolson method; direct Lyapunov method; Lyapunov functional
Mathematics Subject Classification: 92D25, 92D30, 65M06

1. Introduction

The origins of mathematical modeling for viral infections date back to Daniel Bernoulli's work in the late 18th century [1]. In contrast, mathematical modeling specifically for the human immunodeficiency virus (HIV) emerged more recently, in the mid-20th century [2,3]. The first aspects of the phases of the HIV viral cycle that were modeled were viral replication, infection, and cell death in the basic model of viral infection [2, 4]. Excellent reviews have been published on modeling with ordinary differential equations of different aspects of HIV infection [3, 5] in response to the efficacy of antiretroviral therapy, differential drug effects, cell-mediated immunity, and the inclusion of quiescent, chronically infected, and latently infected cells.

Historically, Kermack and McKendrick [6] developed some of the earliest age-structured models for infectious diseases using hyperbolic partial differential equations (PDEs) in 1927. In 1986, Anderson et al. [7] formulated age-structured models for the spread of HIV at the population level. Later, in 1986, Kirschner proposed age-structured models for viral infection at the cellular level using hyperbolic PDEs for HIV. These models account for the age of cellular infection, defined as the time elapsed since a cell became infected with HIV [8]. Subsequently, Nelson and collaborators proposed an age-structured model of HIV infection that allows for variations in the death rate of productively infected cells and the production rate of viral particles [9]. Rong and collaborators [10] analyzed the local analysis of the equilibrium points (virus-free and infected equilibria) and numerical simulations of the solutions. Later on, the development of techniques to construct Volterra-type Lyapunov functionals for age-structured models by McCluskey et al. [11, 12] and Korobenikov [13] contributed to the work of Huang [14] and collaborators, who solved the problem of the global stability of the solutions for the basic model of viral infections with the age of cellular infection.

Many parts of the viral life cycle of HIV remain elusive. The beginning of viral transcription, which is controlled by the regulatory protein trans-activator of transcription (Tat), creates a positive feedback loop, and is one of the most important phases. Althaus and De Boer incorporated the transactivation circuit [15] into a comprehensive model of virus dynamics that accounts for viral infection, replication, and cell death. $I(t) = \int_0^{+\infty} i(a,t)\,da$ is the total concentration of recently infected cells, where $i(\cdot,t)$ denotes the infection-age density at time t. $A(t)$, $L(t)$, and $V(t)$ are the concentrations of activated virus-producing cells, latently infected cells, and free virus particles, respectively. The model is the following:

$$\begin{aligned}
\frac{\partial i(a,t)}{\partial t} + \frac{\partial i(a,t)}{\partial a} &= -s(a)i(a,t),\\
\frac{dA(t)}{dt} &= \int_0^{+\infty} s(a)i(a,t)da - rA(t) + \eta L(t) - \delta A(t),\\
\frac{dL(t)}{dt} &= rA(t) - \eta L(t) - \mu L(t),\\
\frac{dV(t)}{dt} &= pA(t) - cV(t),\\
i(a,0) &= i_0(a),\\
i(0,t) &= \lambda T V(t).
\end{aligned} \tag{1.1}$$

The expression $\int_{a_1}^{a_2} i(a,t)\,da$ gives the concentration of recently infected cells with ages between

a_1 and a_2 at time t. The initial condition $i_0(a)$ refers to the initial distribution of recently infected cells with transactivation-age, while $i(0,t)$ represents the infected cells of age zero that are created by infection. The initial conditions of activated virus-producing cells, latently infected cells, and free virus particles are non-negative: A_0, L_0, and V_0, respectively. Here, T is the constant population of uninfected cells, which become infected at a rate λ per target cell per free-virus particle. The activated virus-producing cells $A(t)$ are generated through the age-dependent transactivation rate $s(a)$, which describes the activation of recently infected cells early after infection at a rate depending on the age a. Additionally, $A(t)$ is generated by the activation of latently infected cells at a rate η, while being decreased by a constant reversion rate r of latently infected cells, and they die at a rate δ per day, independent of the age of infection. Latently infected cells, $L(t)$, are generated through the reversion of activated cells r and can either become activated at a rate η and die at a rate μ. The free-virus particles $V(t)$ are generated by the infected cells producing virions $A(t)$ at a rate p, with clearance at a rate c.

We investigated a modified version that considers the dynamics of the uninfected cells and applies them to the mathematical model presented in Althaus and De Boer [15]

$$\begin{aligned}
\frac{dT(t)}{dt} &= \psi - \gamma T(t) - \lambda T(t)V(t),\\
\frac{\partial i(a,t)}{\partial t} + \frac{\partial i(a,t)}{\partial a} &= -s(a)i(a,t),\\
\frac{dA(t)}{dt} &= \int_0^{+\infty} s(a)i(a,t)da - rA(t) + \eta L(t) - \delta A(t),\\
\frac{dL(t)}{dt} &= rA(t) - \eta L(t) - \mu L(t),\\
\frac{dV(t)}{dt} &= pA(t) - cV(t),\\
i(0,t) &= \lambda T(t)V(t).
\end{aligned} \tag{1.2}$$

The model (1.2) assumes that uninfected cells $T(t)$ are created at a constant rate ψ and die at a rate γ. The dynamics of uninfected cells $T(t)$ in models of viral dynamics have been widely considered in previous works [2–5, 9, 10]. Recently, significant advances have been made in the development of numerical schemes for solving mathematical models describing infection dynamics, particularly those governed by hyperbolic and parabolic partial differential equations. Arif et al. [16] addressed a fractional one-dimensional heat equation using an implicit finite difference method combined with a Lyapunov-based stability analysis, while in [17], they proposed a collocation method based on shifted Jacobi polynomials to solve time-fractional wave equations, demonstrating spectral accuracy and efficiency for fractional dynamics. These numerical methods have proven effective in biomedical applications, such as the spread of infection and anomalous diffusion processes. In the specific context of viral dynamics, hyperbolic PDEs with an age–structure, such as the model considered in this study, often require robust numerical approaches due to the stiff and multi-scale nature of the system. Webb [18] applied semigroup theory to study the dynamics of structured population models, and Diekmann et al. [19] introduced renewal equations as a foundation for modern numerical approaches. In bacterial population models, Abia et al. [20] conducted a comparative analysis of first-order upwind finite difference schemes, characteristic-based methods, and Runge–Kutta schemes for the time integration of ordinary differential equations (ODEs), highlighting the effectiveness of

the method of characteristics in reducing the numerical diffusion associated with hyperbolic PDEs. Building on these developments, we implement a Crank–Nicolson scheme for the discretization of the hyperbolic PDE with respect to the infection–age variable and employ a fourth-order Runge–Kutta method for the coupled ODEs.

In the following, we assume that $s(a)$ is a positive, bounded, and integrable function, and that the initial conditions are given by

$$i(a,0) = i_0(a), \quad T(0) = T_0, \quad A(0) = A_0, \quad L(0) = L_0, \quad V(0) = V_0, \tag{1.3}$$

where T_0, A_0, L_0, and V_0 are the initial uninfected cells, activated virus-producing cells, latently infected cells and free-virus particles, respectively. We assume that $(i_0(a), V_0) \neq (0_{L^1}, 0_{\mathbf{R}})$, that is, they are not equal to zero simultaneously. Althaus and De Boer [15] proposed the following dependent transactivation rate:

$$s(a) = \frac{\widehat{s}(a)}{1 - \int_0^a \widehat{s}(\tau)\, d\tau}, \tag{1.4}$$

where $\widehat{s}(a)$ is the probability density function and $\int_0^a \widehat{s}(\tau)\, d\tau$ is the cumulative probability density function of transactivation. To ensure that the function $s(a)$ does not diverge as $a \to \infty$, certain conditions must be imposed on $\widehat{s}(a)$:

(i) The function $\widehat{s}(a)$ should decay sufficiently fast as a becomes large; specifically, $\widehat{s}(a) \sim \frac{C}{a^p}$ for some $p > 1$, where C is a positive constant.

(ii) Additionally, $\widehat{s}(a)$ is defined for $a > 0$ and remains bounded as $a \to 0^+$.

The paper is organized as follows: The model's basic properties and the global asymptotic stability of virus-free and infected equilibria using the direct Lyapunov method with Volterra-type Lyapunov functionals, are presented in Section 2. We adopt the techniques for the construction of Volterra-type Lyapunov functionals developed in the references [11–14]. In Section 3, we present numerical simulations in each of the two settings for R_0 to illustrate the theoretical results. In Section 4, we present both global and local sensitivity analyses. In Section 5, we discuss the theoretical results and their implications for infection control. The paper ends with concluding remarks in Section 6.

2. Qualitative analysis of the model

2.1. Existence, non-negativity, and boundedness of solutions

Let

$$\Omega = \left\{(T(t), i(a,t), A(t), L(t), V(t)) \in \mathbf{R}_{\geq 0} \times L^1_+((0,+\infty), \mathbf{R}) \times \mathbf{R}_{\geq 0} \times \mathbf{R}_{\geq 0} \times \mathbf{R}_{\geq 0}\right\}$$

be the phase space of the system (1.2) phase space.

With the boundary conditions $i(0,t) = \lambda T(t)V(t)$ and the initial conditions in (1.3), we find that $i(a,t)$ is given by

$$i(a,t) = \begin{cases} \lambda T(t-a)V(t-a) \exp\left(-\int_0^a s(\tau)\, d\tau\right), & \text{for } t > a \geq 0, \\ i_0(a-t) \exp\left(-\int_0^t s(a-t+\tau)\, d\tau\right), & \text{for } a \geq t > 0. \end{cases} \tag{2.1}$$

Note that $\lim_{a\to\infty} i(a,t) = 0$ for any $t \le a$. Using the existence and uniqueness theorem for functional differential equations (Theorems 2.1 and 2.2 in Kuang [21]), it is seen that the system (1.2) in which $i(a,t)$ is substituted, the expression from (2.1) has a unique solution, which is globally defined for all $t \ge 0$. This proof is based on the existence and uniqueness results obtained in [14].

We study the existence of positive solutions of (1.2). By Eq (2.1), we note that $i(a,t)$ remains non-negative for non-negative initial conditions. Furthermore, suppose a time $t_1 \ge 0$ exists such that $T(t_1) = 0$ and $T(t) > 0$ for $0 \le t < t_1$. Then, from the first equation in (1.2) we have $\frac{dT(t_1)}{dt} = \psi > 0$. Hence, $T(t) \ge 0$ for all $t \ge 0$. Similarly, we can show that $A(t) \ge 0$, $L(t) \ge 0$, and $V(t) \ge 0$ for all $t \ge 0$ for all positive initial conditions. This proof is based on the results concerning the existence of positive solutions obtained in [14]. Hence, the result follows.

Proposition 2.1. *System (1.2) has a unique non-negative solution for non-negative initial conditions.*

We consider the boundedness of the solutions of system (1.2). Let $(T(t), i(a,t), A(t), L(t), V(t))$ be any solution with non-negative initial conditions (1.3). We define a functional

$$B(t) = T(t) + \int_0^{+\infty} i(a,t)da + \frac{n}{n+1}A(t) + \frac{n}{n+1}L(t) + \frac{\delta(n-1)}{p(n+1)}V(t),\ n \gg 1. \tag{2.2}$$

The time derivative along the solution of (2.2) is

$$\begin{aligned}\frac{dB(t)}{dt} &= \psi - \gamma T(t) - \lambda T(t)V(t)\\ &\quad - \int_0^{+\infty}\left(\frac{\partial i(a,t)}{\partial a} + s(a)i(a,t)\right)da\\ &\quad + \frac{n}{n+1}\int_0^{+\infty} s(a)i(a,t)da - \frac{n\mu}{n+1}L(t)\\ &\quad - \frac{n\delta}{n+1}A(t) - \frac{c\delta(n-1)}{p(n+1)}V(t).\end{aligned} \tag{2.3}$$

By integrating, we get

$$\int_0^{+\infty}\frac{\partial i(a,t)}{\partial a}da = [i(a,t)]_{a=0}^{a=+\infty} = [i(a,t)]_{a=+\infty} - \lambda T(t)V(t). \tag{2.4}$$

Using Eq (1.4), we have $\int_0^{+\infty} s(a)i(a,t)da \le k\int_0^{+\infty} i(a,t)da$ for some $k > 0$. Combining this with Eq (2.4), we obtain:

$$\frac{dB(t)}{dt} \le \psi - \gamma T(t) - \frac{k}{n+1}\int_0^{+\infty} i(a,t)da - \mu\cdot\frac{n}{n+1}L(t) - \frac{\delta}{n}\cdot\frac{n}{n+1}A(t) - c\cdot\frac{\delta(n-1)}{p(n+1)}V(t).$$

It follows that

$$\frac{dB(t)}{dt} + \eta B(t) \leq \psi, \tag{2.5}$$

where $\eta = \min\left\{\gamma, \frac{k}{n+1}, \mu, \frac{\delta}{n}, c\right\}$. The inequality (2.5) will then follow by a standard comparison theorem; we can conclude that $\limsup_{t\to\infty} B(t) \leq \frac{\psi}{\eta}$. Therefore, $T(t)$, $i(a,t)$, $A(t)$, $L(t)$ and $V(t)$ are all bounded for all $t \geq 0$.

Proposition 2.2. *Let $(T(t), i(a,t), A(t), L(t), V(t))$ be the solution of the model (1.2) with the initial conditions (1.3). Then $T(t)$, $i(a,t)$, $A(t)$, $L(t)$, and $V(t)$ remain bounded for all $t \geq 0$ for which the solution exists.*

The following result is a direct consequence of Proposition (2.2).

Proposition 2.3. *If $(T(0), i(a,0), A(0), L(0), V(0))$ and $B(t) \leq K$ for some $K \geq \frac{\psi}{\eta}$, then $T(t) \leq K$ with $\int_0^{+\infty} i(a,t)da \leq K$, $A(t) \leq K$, $L(t) \leq K$, $V(t) \leq K$ for all $t \geq 0$.*

2.2. Equilibria and their stability results

Now we calculate the equilibrium points of the system (1.2) based on the following system:

$$\begin{aligned}
\psi &= \gamma T^* + \lambda T^* V^*, && (2.6)\\
\frac{di^*(a)}{da} &= -s(a) i^*(a), && (2.7)\\
\int_0^{+\infty} s(a) i^*(a) da &= (r+\delta) A^* - \eta L^*, && (2.8)\\
rA^* &= (\eta + \mu) L^*, && (2.9)\\
pA^* &= cV^*, && (2.10)\\
i^*(0) &= \lambda T^* V^*. && (2.11)
\end{aligned}$$

This gives two equilibria. The first is $E^0 = (T^0, 0, 0, 0, 0)$, where $T^0 = \psi/\gamma$, which represents the state in which there is no infection and we refer to this as the virus-free equilibrium. The second equilibrium $E^* = (T^*, i^*(a), A^*, L^*, V^*)$ is the state where the virus can establish an infection and is known as the infected equilibrium [22]. The coordinates of positive equilibrium are

$$\begin{gathered}
T^* = \tfrac{T^0}{R_0}, \;\; i^*(a) = \rho(a)\tfrac{\gamma T^0}{R_0}(R_0 - 1), \;\; A^* = \tfrac{c\gamma}{p\lambda}(R_0 - 1),\\
L^* = \tfrac{cr\gamma}{p(\eta+\mu)\lambda}(R_0 - 1), \;\; \text{and} \;\; V^* = \tfrac{\gamma}{\lambda}(R_0 - 1),
\end{gathered}$$

where

$$\rho(a) = \exp\left(-\int_0^a s(\phi)d\phi\right),$$

$$\begin{aligned} \sigma &= \int_0^{+\infty} s(a)\rho(a)da, \\ R_0 &= \frac{\psi p\sigma\lambda(\eta+\mu)}{\gamma c\left[(\eta+\mu)(r+\delta)-\eta r\right]}. \end{aligned} \tag{2.12}$$

R_0 is the basic reproduction number, as it describes the average number of secondary infected cells generated by each infected cell at the onset of the infection. The infected equilibrium exists and is positive if $R_0 > 1$. Accordingly, we have the following result.

Theorem 2.1. *If $R_0 > 1$, then the system (1.2) admits a unique infected (positive) equilibrium E^* in the interior of the positive orthant.*

The global properties of the system (1.2) are given in the following theorem.

Theorem 2.2. *For the system (1.2), (i) if $R_0 \leq 1$, the virus-free equilibrium E^0 is globally asymptotically stable in the non-negative orthant; (ii) if $R_0 > 1$, then the infected equilibrium E^* is globally asymptotically stable in the interior of the positive orthant.*

Proof. First, we define a positive function as in [11, 14]

$$\kappa(a) = \int_a^{+\infty} s(v)\exp\left(-\int_a^v s(\phi)d\phi\right)dv. \tag{2.13}$$

Note that $\kappa(a) > 0$ for $0 \leq a < +\infty$, and (2.13) satisfies $\kappa(0) = \sigma$.

The derivative of $\kappa(a)$ satisfies

$$\begin{aligned} \kappa'(a) &= \kappa(a)s(a) - \exp\left(\int_0^a s(\phi)d\phi\right)\cdot s(a)\cdot\exp\left(-\int_0^a s(\phi)d\phi\right), \\ \kappa'(a) &= \kappa(a)s(a) - s(a). \end{aligned} \tag{2.14}$$

Second, to demonstrate stability, the following lemma is necessary:

Lemma 2.3. *The function [11–14]*

$$J(x) = x - 1 - \ln x. \tag{2.15}$$

is defined positive in $\mathbf{R}_{0+}$.

We will utilize $\kappa(a)$, $\kappa'(a)$, and $J(x)$ to demonstrate the global stability of the equilibrium points.

(i) For the virus-free equilibrium E^0, we consider a Volterra-type Lyapunov functional

$$W(t) = \sigma T^0 J\left(\frac{T(t)}{T^0}\right) + \int_0^{+\infty}\kappa(a)i(a,t)da + A(t) + \frac{\eta}{\eta+\mu}L(t) + \frac{\lambda\sigma T^0}{cR_0}V(t).$$

By using $\psi = \gamma T^0$ and (2.12), we have

$$\frac{dW}{dt} = \sigma\psi\left(2 - \frac{T(t)}{T^0} - \frac{T^0}{T(t)}\right) - \sigma\lambda T(t)V(t)$$
$$- \int_0^{+\infty} \kappa(a)\frac{\partial i(a,t)}{\partial a}da - \int_0^{+\infty}(\kappa(a)s(a) - s(a))i(a,t)da + \left[\sigma\lambda T^0 - \frac{\sigma\lambda T^0}{R_0}\right]V(t).$$

Integrating by parts and using $\kappa(0) = \sigma$, $i(0,t) = \lambda T(t)V(t)$, and (2.14), we have

$$\int_0^{+\infty} \kappa(a)\frac{\partial i(a,t)}{\partial a}da = [\kappa(a)i(a,t)]_{a=0}^{a=+\infty} - \int_0^{+\infty}\kappa'(a)i(a,t)da,$$
$$= [\kappa(a)i(a,t)]_{a=+\infty} - \sigma\lambda T(t)V(t) - \int_0^{+\infty}(\kappa(a)s(a) - s(a))i(a,t)da.$$

Substituting the above expression in dW/dt, we have

$$\frac{dW}{dt} = -\sigma\psi\left[J\left(\frac{T(t)}{T^0}\right) + J\left(\frac{T^0}{T(t)}\right)\right] - [\kappa(a)i(a,t)]_{a=+\infty} - \frac{\sigma\lambda T^0}{R_0}\left[1 - R_0\right]V(t).$$

That is, $\frac{dW}{dt} \leq 0$ holds for all $R_0 \leq 1$. Furthermore, for $R_0 < 1$, equality $\frac{dW}{dt} = 0$ holds only on the set

$$\{(T, i(a,t), A, L, V) \geq 0 \,|\, T(t) = T^0, i(a,t) = 0, V(t) = 0\}.$$

When $R_0 = 1$, $\frac{dW}{dt} = 0$ if and only if

$$\{(T, i(a,t), A, L, V) \geq 0 \,|\, T(t) = T^0, i(a,t) = 0\}.$$

It is simple to observe that this set is transversal to the phase flow everywhere but a single point E^0. Therefore, by LaSalle's invariance principle, the condition $R_0 \leq 1$ is necessary and sufficient to ensure the global stability of the virus-free equilibrium E^0.

(*ii*) The existence of the infected equilibrium E^* for $R_0 > 1$ is proved above. We consider the following functional to prove its global stability:

$$U(t) = \sigma T^* J\left(\frac{T(t)}{T^*}\right) + \int_0^{+\infty}\left[\kappa(a)i^*(a)J\left(\frac{i(a,t)}{i^*(a)}\right)\right]da + A^*J\left(\frac{A(t)}{A^*}\right) + BL^*J\left(\frac{L(t)}{L^*}\right) + CV^*J\left(\frac{V(t)}{V^*}\right),$$

where

$$B = \frac{\eta L^*}{rA^*}, \;\; C = \frac{\sigma\lambda T^* V^*}{pA^*}.$$

At the infected equilibrium, we have

$$\psi = \gamma T^* + \lambda T^* V^*, \tag{2.16}$$

$$(\delta + r)A^* = \sigma\lambda T^* V^* + \eta L^*, \tag{2.17}$$
$$(\eta + \mu)L^* = rA^*, \tag{2.18}$$
$$cV^* = pA^*. \tag{2.19}$$

Let $U_1(t) = \sigma T^* J\left(\frac{T(t)}{T^*}\right) + A^* J\left(\frac{A(t)}{A^*}\right) + BL^* J\left(\frac{L(t)}{L^*}\right) + CV^* J\left(\frac{V(t)}{V^*}\right)$. By using (2.16) and (2.19), we obtain

$$\begin{aligned}
\frac{dU_1}{dt} &= \sigma\left(1 - \frac{T^*}{T(t)}\right)\left(\gamma T^*\left(1 - \frac{T(t)}{T^*}\right) + \lambda T^* V^*\left(1 - \frac{T(t)V(t)}{T^*V^*}\right)\right) \\
&+ \left(1 - \frac{A^*}{A(t)}\right)\left(\int_0^{+\infty} s(a)i(a,t)da - \sigma\lambda T^* V^* \frac{A(t)}{A^*} + \eta L^*\left(\frac{L(t)}{L^*} - \frac{A(t)}{A^*}\right)\right) \\
&+ \frac{\eta L^*}{rA^*} rA^*\left(1 - \frac{L^*}{L(t)}\right)\left(\frac{A(t)}{A^*} - \frac{L(t)}{L^*}\right) \\
&+ \frac{\sigma\lambda T^* V^*}{pA^*} pA^*\left(1 - \frac{V^*}{V(t)}\right)\left(\frac{A(t)}{A^*} - \frac{V(t)}{V^*}\right), \\
&= \sigma\gamma T^*\left(2 - \frac{T^*}{T(t)} - \frac{T(t)}{T^*}\right) + \sigma\lambda T^* V^*\left(1 - \frac{T(t)V(t)}{T^*V^*} - \frac{T^*}{T(t)} + \frac{V(t)}{V^*}\right) \\
&+ \int_0^{+\infty} s(a)i(a,t)da - \frac{A^*}{A(t)}\int_0^{+\infty} s(a)i(a,t)da + \sigma\lambda T^* V^* - \sigma\lambda T^* V^* \frac{A(t)}{A^*} \\
&+ \eta L^*\left(\frac{L(t)}{L^*} - \frac{A(t)}{A^*} - \frac{A^* L(t)}{A(t)L^*} + 1\right) \\
&+ \eta L^*\left(\frac{A(t)}{A^*} - \frac{L(t)}{L^*} - \frac{A(t)L^*}{A^* L(t)} + 1\right) \\
&+ \sigma\lambda T^* V^*\left(\frac{A(t)}{A^*} - \frac{V(t)}{V^*} - \frac{A(t)V^*}{A^* V(t)} + 1\right), \\
&= \sigma\gamma T^*\left(2 - \frac{T^*}{T(t)} - \frac{T(t)}{T^*}\right) + \eta L^*\left(2 - \frac{A^* L(t)}{A(t)L^*} - \frac{A(t)L^*}{A^* L(t)}\right) \\
&+ \int_0^{+\infty} i^*(a)s(a)\left(\frac{i(a,t)}{i^*(a)} - \frac{i(a,t)A^*}{i^*(a)A(t)}\right)da + \sigma\lambda T^* V^*\left(3 - \frac{A(t)V^*}{A^* V(t)} - \frac{T(t)V(t)}{T^*V^*} - \frac{T^*}{T(t)}\right).
\end{aligned} \tag{2.20}$$

Let $U_2(t) = \int_0^{+\infty}\left[\kappa(a)i^*(a)J\left(\frac{i(a,t)}{i^*(a)}\right)\right]da$. We have

$$\frac{dU_2}{dt} = \int_0^{+\infty}\kappa(a)\left(1 - \frac{i^*(a)}{i(a,t)}\right)\frac{\partial i(a,t)}{\partial t}da = -\int_0^{+\infty}\kappa(a)\left(1 - \frac{i^*(a)}{i(a,t)}\right)\left(\frac{\partial i(a,t)}{\partial a} + s(a)i(a,t)\right)da.$$

Note that

$$\frac{\partial}{\partial a}J\left(\frac{i(a,t)}{i^*(a)}\right) = \left(1 - \frac{i^*(a)}{i(a,t)}\right)\left(\frac{\partial_a i(a,t)}{i^*(a)} - \frac{i(a,t)\cdot D[i^*(a)]}{i^*(a)i^*(a)}\right),$$

where $\partial_a i(a,t)$ denotes $\frac{\partial i(a,t)}{\partial a}$, and $D[i^*(a)]$ denotes $\frac{di^*(a)}{da}$.

Using the equation in (2.7), we have:

$$i^*(a)\frac{\partial}{\partial a}J\left(\frac{i(a,t)}{i^*(a)}\right) = \left(1-\frac{i^*(a)}{i(a,t)}\right)(\partial_a i(a,t) + s(a)i(a,t)).$$

We have

$$\frac{dU_2}{dt} = -\int_0^{+\infty} \kappa(a)i^*(a)\frac{\partial}{\partial a}J\left(\frac{i(a,t)}{i^*(a)}\right)da. \tag{2.21}$$

Hence, using integration by parts, we have

$$\begin{aligned}\int_0^{+\infty} \kappa(a)i^*(a)\frac{\partial}{\partial a}J\left(\frac{i(a,t)}{i^*(a)}\right)da &= \left[\kappa(a)i^*(a)J\left(\frac{i(a,t)}{i^*(a)}\right)\right]_{a=0}^{a=+\infty} - \int_0^{+\infty}\frac{d}{da}\left[\kappa(a)i^*(a)\right]J\left(\frac{i(a,t)}{i^*(a)}\right)da,\\ &= \left[\kappa(a)i^*(a)J\left(\frac{i(a,t)}{i^*(a)}\right)\right]_{a=0}^{a=+\infty} - \int_0^{+\infty}\left[\kappa'(a)i^*(a)+\kappa(a)D[i^*(a)]\right]J\left(\frac{i(a,t)}{i^*(a)}\right)da.\end{aligned}$$

Using the derivative of $\kappa(a)$, we have

$$\begin{aligned}\int_0^{+\infty} \kappa(a)i^*(a)\frac{\partial}{\partial a}J\left(\frac{i(a,t)}{i^*(a)}\right)da &= \left[\kappa(a)i^*(a)J\left(\frac{i(a,t)}{i^*(a)}\right)\right]_{a=+\infty} - \left[\kappa(0)i^*(0)J\left(\frac{i(0,t)}{i_h^*(0)}\right)\right]\\ &\quad - \int_0^{+\infty}\left[i^*(a)\kappa(a)s(a) - i^*(a)s(a) + \kappa(a)D[i^*(a)]\right]J\left(\frac{i(a,t)}{i^*(a)}\right)da\end{aligned}$$

and used the following equalities:

$$\kappa(0) = \sigma,\ \ i^*(0) = \lambda T^*V^*\ \ i(0,t) = \lambda T(t)V(t)\ \text{ and }\ D[i^*(a)] = -s(a)i^*(a).$$

We have

$$\begin{aligned}\int_0^{+\infty} \kappa(a)i^*(a)\frac{\partial}{\partial a}J\left(\frac{i(a,t)}{i^*(a)}\right)da &= \left[\kappa(a)i^*(a)J\left(\frac{i(a,t)}{i^*(a)}\right)\right]_{a=+\infty} - \left[\sigma\lambda T^*V^*J\left(\frac{T(t)V(t)}{T^*V^*}\right)\right]\\ &\quad + \int_0^{+\infty} i^*(a)s(a)J\left(\frac{i(a,t)}{i^*(a)}\right)da.\end{aligned} \tag{2.22}$$

Substituting the expression (2.22) in (2.21), we have

$$\begin{aligned}\frac{dU_2}{dt} &= -\left[\kappa(a)i^*(a)J\left(\frac{i(a,t)}{i^*(a)}\right)\right]_{a=+\infty} + \sigma\lambda T^*V^*\left[\frac{T(t)V(t)}{T^*V^*} - 1 - \ln\frac{T(t)V(t)}{T^*V^*}\right]\\ &\quad - \int_0^{+\infty} i^*(a)s(a)\left[\frac{i(a,t)}{i^*(a)} - 1 - \ln\frac{i(a,t)}{i^*(a)}\right]da.\end{aligned} \tag{2.23}$$

Combining (2.20) and (2.23), we have

$$\frac{dU}{dt} = \sigma\gamma T^*\left(2 - \frac{T^*}{T(t)} - \frac{T(t)}{T^*}\right) + \eta L^*\left(2 - \frac{A^*L(t)}{A(t)L^*} - \frac{A(t)L^*}{A^*L(t)}\right) - \left[\kappa(a)i^*(a)J\left(\frac{i(a,t)}{i^*(a)}\right)\right]_{a=+\infty}$$
$$- \int_0^{+\infty} i^*(a)s(a)\left(\frac{i(a,t)A^*}{i^*(a)A(t)} - 1 - \ln\frac{i(a,t)}{i^*(a)}\right)da$$
$$- \sigma\lambda T^*V^*\left(\frac{T^*}{T(t)} - 1 - \ln\frac{T^*}{T(t)} + \frac{A(t)V^*}{A^*V(t)} - 1 - \ln\frac{A(t)V^*}{A^*V(t)} - \ln\frac{A^*}{A(t)}\right).$$

We know that $\int_0^{+\infty} i^*(a)s(a)da = \sigma\lambda T^*V^*$. Finally

$$\frac{dU}{dt} = -\sigma\gamma T^*\left[J\left(\frac{T^*}{T(t)}\right) + J\left(\frac{T(t)}{T^*}\right)\right] - \eta L^*\left[J\left(\frac{A^*L(t)}{A(t)L^*}\right) + J\left(\frac{A(t)L^*}{A^*L(t)}\right)\right] - \left[\kappa(a)i^*(a)J\left(\frac{i(a,t)}{i^*(a)}\right)\right]_{a=+\infty}$$
$$- \int_0^{+\infty} i^*(a)s(a)J\left(\frac{i(a,t)A^*}{i^*(a)A(t)}\right)da - \sigma\lambda T^*V^*\left[J\left(\frac{T^*}{T(t)}\right) + J\left(\frac{A(t)V^*}{A^*V(t)}\right)\right].$$

Since $J(x) \geq 0$ for every $x > 0$, and given the existence of the infected equilibrium E^* then $\frac{dU}{dt} \leq 0$ holds everywhere in the interior of the positive orthant. The equality $\frac{dU}{dt} = 0$ holds only on the set

$$M = \{(T, i(a,t), A, L, V) > 0 \mid T(t) = T^*, i(a,t) = i^*(a), A(t) = A^*, L(t) = L^*, V(t) = V^*\}.$$

The infected equilibrium E^* is easily observed to be the only invariant set of the system (1.2) in M. As a result, this equilibrium is globally asymptotically stable in the interior of the positive orthant according to LaSalle's invariance principle. □

Uniform persistence is a classical analysis in micro- or macro-epidemiological models when the basic reproductive number is greater than 1. For system the (1.2), it is necessary to study the persistence of viruses when $R_0 > 1$. The idea of the proof is omitted, as it is similar to the methods used in [23].

Theorem 2.4. *If $R_0 > 1$, then the system (1.2) is uniformly persistent.*

3. Numerical solutions

In this section, we present the results of the numerical solution of the model (1.2), which involves solving a coupled system of differential equations. This system consists of four ODEs for the variables $T(t)$, $A(t)$, $L(t)$, and $V(t)$, along with a PDE for the unknown function $i(a,t)$. In the following subsections, we provide detailed information on the numerical methods used for discretizing the model, its implementation, the parameter values, and the simulations conducted for each case.

3.1. Model discretization

We apply the fourth-order Runge–Kutta method to solve the ODE part of the model; the PDE is solved with the Crank–Nicolson finite difference method. The equations are discretized in both time

and age as appropriate. Since the third equation in (1.2) involves an integral over the age domain, we employ the trapezoidal rule as a numerical integration technique to approximate it.

Regarding the age-domain, although $i(a,t)$ is theoretically defined over $[0,\infty)$, for numerical purposes, we truncate this domain to $[0,a_f]$, where a_f is chosen to be sufficiently large to approximate infinity. The numerical approximations for $T(t)$, $A(t)$, $L(t)$, and $V(t)$ are computed over the interval $[0,t_f]$, while the function $i(a,t)$ is evaluated over the truncated domain $[0,a_f]\times[0,t_f]$, where t_f represents the final time. Each of the terms that appear in the PDE of the model (1.2) is approximated as follows [24–26]:

$$\frac{\partial i(a,t)}{\partial t}\Big|_{a=a_j,t=t^k} = \frac{\mathrm{i}_j^{k+1}-\mathrm{i}_j^k}{\Delta t}+O(\Delta t), \tag{3.1}$$

$$\frac{\partial i(a,t)}{\partial a}\Big|_{a=a_j,t=t^k} = \frac{1}{2}\left(\frac{\mathrm{i}_{j+1}^k-\mathrm{i}_{j-1}^k}{2\Delta a}+\frac{\mathrm{i}_{j+1}^{k+1}-\mathrm{i}_{j-1}^{k+1}}{2\Delta a}\right)+O(\Delta a^2), \tag{3.2}$$

$$s(a)i(a,t)\Big|_{a=a_j,t=t^k} = \frac{1}{2}S_j\left(\mathrm{i}_j^k+\mathrm{i}_j^{k+1}\right)+O(\Delta t). \tag{3.3}$$

The discretization of the PDE is achieved by replacing each term with its corresponding approximation (3.1)–(3.3), leading to the following equation:

$$\frac{\mathrm{i}_j^{k+1}-\mathrm{i}_j^k}{\Delta t}+\frac{1}{4\Delta a}\left(\mathrm{i}_{j+1}^k-\mathrm{i}_{j-1}^k+\mathrm{i}_{j+1}^{k+1}-\mathrm{i}_{j-1}^{k+1}\right)=-\frac{1}{2}S_j(\mathrm{i}_j^k+\mathrm{i}_j^{k+1}),\quad j=1,\dots,N,\ k=0,\dots,M. \tag{3.4}$$

Since this finite difference scheme is implicit [25, 27], this leads to solving the following system of equations for the unknowns i_j^{k+1}, $j=1,\dots,N$:

$$-\zeta\mathrm{i}_{j-1}^{k+1}+\left(1+\frac{\Delta t}{2}S_j\right)\mathrm{i}_j^{k+1}+\zeta\mathrm{i}_{j+1}^{k+1}=\zeta\mathrm{i}_{j-1}^k+\left(1-\frac{\Delta t}{2}S_j\right)\mathrm{i}_j^k-\zeta\mathrm{i}_{j+1}^k,\quad j=1,\dots,N,\ k=0,\dots,M, \tag{3.5}$$

where $\zeta=\Delta t/(4\Delta a)$. Here, i_j^k and S_j represent the numerical approximations to $i(a_j,t^k)$ and $s(a_j)$, respectively. From Eq (3.5), it is important to distinguish that for $k=0$, we refer to the initial condition, which is denoted as $\mathrm{i}_j^0=i_0(a_j)$ (values indicated in Table 1). Similarly, for $j=1$, we are addressing the boundary condition at $a=0$, i.e., $\mathrm{i}_0^k=\lambda T(t^k)V(t^k)$. This last condition must be taken into account from the first time level onwards, since the evolution of $i(a_j,t^{k+1})$ in each time step depends on the value of this condition. On the other hand, the discretization of the ODEs of the model using the fourth-order Runge–Kutta method is as follows [28, 29]:

$$X^{k+1}=X^k+\frac{\Delta t}{6}\sum_{j=1}^{4}\varsigma_j\chi_j^k, \tag{3.6}$$

where X represents any of the variables T, V, A, or L. The coefficients ς_j are: $\varsigma_1=1$, $\varsigma_2=2$, $\varsigma_3=2$, and $\varsigma_4=1$. The terms χ_j^k, $j=1,\dots,4$ are defined as

$$\chi_j^k=\begin{cases} g_j^k, & \text{if } X=T,\\ m_j^k, & \text{if } X=V,\\ w_j^k, & \text{if } X=A,\\ \phi_j^k, & \text{if } X=L,\end{cases}$$

where

$$\begin{aligned} g_j^k &= f_1(t^k + c_j\Delta t, T^k + d_j\Delta t g_{j-1}^k, V^k + d_j\Delta t m_{j-1}^k), \\ m_j^k &= f_2(t^k + c_j\Delta t, A^k + d_j\Delta t w_{j-1}^k, L^k + d_j\Delta t \phi_{j-1}^k), \\ w_j^k &= f_3(t^k + c_j\Delta t, A^k + d_j\Delta t w_{j-1}^k, L^k + d_j\Delta t \phi_{j-1}^k), \\ \phi_j^k &= f_4(t^k + c_j\Delta t, V^k + d_j\Delta t m_{j-1}^k, A^k + d_j\Delta t w_{j-1}^k). \end{aligned} \tag{3.7}$$

The coefficients c_j and d_j in Eq (3.7) are $d_1 = c_1 = 0$, $d_2 = d_3 = c_2 = c_3 = 1/2$, and $d_4 = c_4 = 1$. The functions $f_1(t^k, T^k, V^k)$, $f_2(t^k, A^k, L^k)$, $f_3(t^k, A^k, L^k)$, and $f_4(t^k, V^k, A^k)$ of Eq (3.7) are given, respectively by

$$f_1(t^k, T^k, V^k) = \psi - \gamma T^k - \lambda T^k V^k, \tag{3.8}$$

$$f_2(t^k, A^k, L^k) = integral - rA^k + \eta L^k - \delta A^k, \tag{3.9}$$

$$f_3(t^k, A^k, L^k) = rA^k - \eta L^k - \mu L^k, \tag{3.10}$$

$$f_4(t^k, V^k, A^k) = pA^k - cV^k. \tag{3.11}$$

The term *integral* in Eq (3.9) is the approximation of the improper integral that appears in the third differential equation of (1.2). The calculation of this term at time level t^k, $k = 1, \ldots, M+1$, relies on the approximations of $T(t)$ and $V(t)$ at time levels t^{k-1} and t^{k+1}. The following subsection presents the details of the numerical implementation of the model's discretization.

3.2. Numerical implementation

This section provides details about the numerical implementation. The graphs and error analysis were conducted using Python on a system equipped with an AMD 16-core Ryzen 9 5950X processor, a GeForce RTX 3090 graphics card, and 32 GB of RAM. The following steps describe the algorithm used to obtain the numerical solution of the model, including the order in which the equations are solved.

(1) *Definition of the input parameters.* The model parameters, including ψ, γ, λ, p, c, r, η, δ, and μ, are defined at the beginning of the code (see Table 1 for their values). The value of p is assigned according to whether the numerical simulation requires $R_0 < 1$ or $R_0 > 1$. Additionally, two positive integers M and N are specified to establish the uniform time step and grid point mesh, respectively.

(2) *Initialization of variables.* The time values are stored in a vector $\mathbf{t}$ of dimension $M+2$, while the grid points are stored in a vector $\mathbf{x}$ of $N+2$ dimensions. The numerical results for the variables of the model are stored in the vectors $\mathbf{T}$, $\mathbf{V}$, $\mathbf{A}$, and $\mathbf{L}$ of $M+2$ dimensions, and a matrix $\mathbf{M}$ of $(M+2)\times(N+2)$ dimensions for $i(a,t)$.

(3) *Age and temporal discretization.* Given M and N, we define a uniform time step as $\Delta t = t_f/(M+1)$ and a uniform grid point mesh $\Delta a = a_f/(N+1)$, where a_f is considered to be a sufficiently large number for numerical purposes. The grid points a_j are indexed by the subscript j, $j = 0, \ldots, N+1$, and the time levels t^k are indexed by the superscript k, $k = 0, \ldots, M+1$. The grid points are distributed as $a_j = j\Delta a$, and the time levels as $t^k = k\Delta t$.

(4) *Initial and boundary conditions*. The initial condition for the variables $T(t)$, $V(t)$, $A(t)$, and $L(t)$ is defined, as well as the initial $i(a,0)$ and the boundary condition $i(0,t)$ for $i(a,t)$. In the code, a function is defined, which will be invoked when assigning the value of the initial condition for each grid point a_j. This information is stored in the first row, starting from the second column of the matrix $\mathbf{M}$.

(5) *Calculation of the basic reproduction number R_0*. Before calculating R_0, the value of σ is obtained, which is determined by numerically evaluating the improper integral that combines the functions $s(a)$ and $\rho(a)$. Then, R_0 is calculated using the parameter values, once σ has been determined.

(6) *The matrix and vector associated with the system of Eq* (3.5). Since the boundary conditions of $i(a,t)$ are already known, the matrix associated with the system (3.5) has $N \times N$ dimensions. The matrix is tridiagonal, with the entries on the main diagonal given by $1 + \frac{\Delta t}{2} S_j$, $j = 1, \ldots, N$; entries on the upper diagonal are given by ζ, and those on the lower diagonal by $-\zeta$. A vector $\mathbf{u}$ of dimension N is created, with the entries given by $\zeta \mathrm{i}_{j-1}^k + \left(1 - \frac{\Delta t}{2} S_j\right) \mathrm{i}_j^k - \zeta \mathrm{i}_{j+1}^k$. This system is solved for each time step.

(7) *Compatibility between the initial and boundary conditions*. To ensure the correct application of the numerical scheme, the compatibility between the initial condition $i(a,0)$, and the boundary condition $i(0,t)$ at $a = 0$ and $t = 0$ will be assumed. For this, according to the information provided in Table 1, it is important to ensure that the boundary condition $i(0,t) = \lambda T(t) V(t)$ aligns with $i(a,0)$ for the specified values of a and t. To establish this compatibility, we assume, for the numerical simulations, that the initial distribution of recently infected cells of transactivation age is $i(a,0) = \lambda T_0 V_0$. Under this assumption, the function $i(a,t)$ is smoothly constructed from $t = 0$, thereby eliminating any inconsistency. With that in mind, the entry in the first row and first column of the matrix $\mathbf{M}$ is given by $\mathbf{M}_{1,1} = \lambda T(0) V(0)$.

(8) *Temporal evolution using the Runge–Kutta method.* Equations (3.7)–(3.11) are defined by separate functions, which are invoked at each time step. The evolution of the solution is calculated from t^1 onward as follows.

- Initialization of the time loop: This loop iterates over the index k for all time steps from t^1 to t^{M+1}.
- Calculation of the term *integral*: Since the integral needs to be evaluated over an infinite domain, for numerical purposes, this domain is truncated, and the values of a_j, $j = 0, \ldots, N+1$ are considered within the domain $[0, a_f]$. An inner loop is initialized that iterates over all grid points a_j. Within each time step, an integral is approximated. First, in the inner loop over j, a temporary value is calculated for each grid point a_j by multiplying the function $s(a_j)$ by the corresponding value in the solution matrix from the previous time step, $\mathbf{M}_{k-1,j}$. Then, the term *integral* is calculated from this set of values by using the trapezoidal rule. In Python, we use the "np.trapz" function from the NumPy module to perform the integration. The *integral* value is used each time the unknown variables of the model are updated.
- Update of the variables T, V, A, and L: We use Eq (3.6) to update T, V, A, and L at time t^k.

- Update the vector $\mathbf{u}$: At time t^k, the first entry of the vector $\mathbf{u}$ is updated as $\mathbf{u}[1]:= \zeta\lambda T^{k-1}V^{k-1} + \left(1 - \frac{\Delta t}{2}s(a_1)\right)\mathbf{M}_{k-1,1} - \zeta\mathbf{M}_{k-1,2} + \zeta\lambda T^k V^k$. For the calculation of $\mathbf{u}$ at the internal grid points, a new loop iterates over all these points and calculates $\mathbf{u}$[j], $j = 2, \ldots, N$ using values from the previous time step. The j-th entry of $\mathbf{u}$ is given by $\mathbf{u}[j] := \zeta\mathbf{M}_{k-1,j} + \left(1 - \frac{\Delta t}{2}s(a_{j+1})\right)\mathbf{M}_{k-1,j+1} - \zeta\mathbf{M}_{k-1,j+2}$.
- Update the matrix $\mathbf{M}$: The system of equations of point 3.2 is solved, and the resulting information for each time t^k is stored in the corresponding row of the matrix $\mathbf{M}$.

Table 1. Initial conditions and parameters of the HIV model (1.2).*

Parameters	Values	Reference
ψ, production rate of uninfected cells	$1.0 \times 10^4/\text{mL} \times \text{day}$	[2]
γ, per-cell death rate of uninfected cell	$0.01/\text{day}$	[2]
λ, rate of infection of uninfected cells	$2.4 \times 10^{-8}/\text{mL} \times \text{day}$	[2]
p, production rate of free virions from an activated infected cell	-	Varying
c, clearance rate of free virus particles (constant)	$23.0/\text{day}$	[2]
r, reversion rate of activated infected cells to latently infected cells	$0.019/\text{day}$	[15]
η, activation rate of latently infected cells to activated infected cells	$0.039/\text{day}$	[15]
δ, per-cell death rate of activated infected cells	$0.7/\text{day}$	[15]
μ, per-cell death rate of latently infected cells	$0.001/\text{day}$	[5]
Initial conditions	**Values**	**Reference**
$T(0)$, initial condition of uninfected target cells	$10 - 10^4/\text{mL}$	Assumed
$V(0)$, initial condition of free virus particles	1.0×10^{-6}	Assumed
$i(a, 0)$, initial condition of recently infected cells	$\lambda T(0)V(0)$*	Assumed
$A(0)$, initial condition of activated infected cells	0	Assumed
$L(0)$, initial condition of latently infected cells	0	Assumed

*Note: See Section 3.2 for more details on the value of this initial condition.

The numerical implementation methodology for the age-structured HIV model is described in Appendix, where the algorithm is presented in structured pseudocode for clarity and reproducibility.

3.3. Parameters for the numerical simulations

We present the values of the parameters used in the model, as well as the initial conditions for the numerical simulations. These are listed in Table 1.

Two simulations are carried out, one for the case when $R_0 = 1.4906 > 1$ and choosing the value $p = 1000$, and another when $R_0 = 0.9689 < 1$ and choosing the value $p = 650$. The function $\widehat{s}(a)$ in (1.4) has been estimated by fitting the distributions of Figures B and C in Ref. [15], which were obtained by Monte–Carlo simulations, to a gamma distribution

$$\widehat{s}(a; \alpha, \beta) = \frac{\beta^\alpha a^{\alpha-1} \exp(-\beta a)}{\Gamma(\alpha)}.$$

For Figure B, we obtained the parameters $\alpha = 8.070335$ and $\beta = 20.289536$, and for Figure C, we obtained $\alpha = 1.543579$ and $\beta = 0.031014$. We define the age-dependent transactivation rates

$s(a)$ as in (1.4). Figure 1 shows the behavior of the transactivation rate $s(a)$, along with its associated probability density function. Two sets of values are given for the parameters of the gamma distribution.

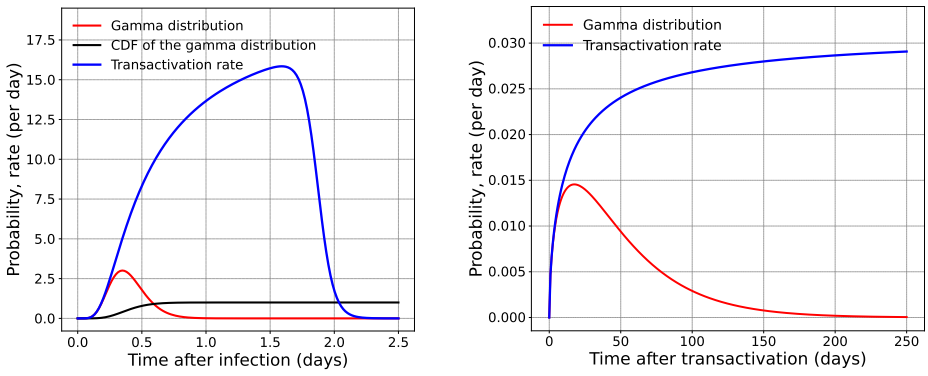

(a) (b)

Figure 1. Dynamics of the transactivation rate $s(a)$. (a) The probability density function and the corresponding rate of transactivation, with gamma distribution parameters $\alpha = 8.070335$ and $\beta = 20.289536$. (b) Probability density function and transactivation rate, with the parameters $\alpha = 1.543579$ and $\beta = 0.031014$.

3.4. Numerical simulations

We carry out numerical simulations of the virus dynamics with an age-dependent transactivation rate, using the numerical solution of the model (1.2). The simulations are to explore the dynamics of the model, with particular focus on the role of the transactivation rate. Different values of the basic reproduction number R_0 are used, a key parameter in determining the system's behavior. These behaviors align with the equilibrium analysis presented in Section 2, and the numerical results provide further insight into the long-term dynamics of the model. Next, we provide details about the numerical solution's convergence and the error estimation to ensure the accuracy and reliability of the results.

3.4.1. Convergence of the numerical solutions

The convergence analysis of finite difference schemes for the solution of differential equations is based on the Lax–Richtmyer theorem [25, 30], which considers the concepts of consistency and stability. To analyze the stability of the Crank–Nicolson method, we generally need to perform a Von Neumann stability analysis. However, note that the model (1.2) includes a function $s(a)$. In this case, it is difficult to find a straightforward analytical stability criterion, so in a practical way, we analyze the stability through numerical experiments.

For this purpose, we perform simulations with different age and time step sizes. We systematically adjust these parameters until achieving an agreement between the numerical solutions and the results of equilibria and stability analyzed in Section 2. In particular, we find that the solutions are stable as long as $\Delta t > \Delta a$; otherwise, spurious solutions [24, 31, 32] are obtained. For the stability of the fourth-order Runge–Kutta method, we require Δt to be small enough. The numerical experiments we carried out indicate that in the time interval $[0, t_f]$, the solutions are stable as long as the time step used

is $\Delta t = t_f/(M+1)$, where $M \geq 2.5t_f$. This condition can be attributed to the stability of the PDE solution.

On the one hand, with $R_0 > 1$, Figure 2 and 3 show that the infection persists as time passes. As $t \to \infty$, it is observed that the solutions stabilize around the coordinates of the equilibrium E^*. When $R_0 < 1$, in Figures 4 and 5, it is observed that the infection gradually dies as time passes. As $t \to \infty$, the solution approaches the virus-free equilibrium E^0, reflecting the clearance of the infection. Figure 6 presents surface plots of the infected cell $i(a,t)$, obtained using the gamma distribution with the parameters $\alpha = 8.070335$ and $\beta = 20.289536$ under both scenarios, $R_0 < 1$ and $R_0 > 1$. These plots reveal how the infection evolves over age and time, thus showing the dynamics of the infection according to the value of the basic reproduction number R_0, which indicates the disease's clearance or persistence. In Figure 7, the dynamics of the infection are shown for the case of the gamma distribution with $\alpha = 1.543579$ and $\beta = 0.031014$. It is evident that the region $(a,t) \in [0,a_f]\times[0,t_f]$ in both figures differs, and this discrepancy arises from the variations in the transactivation rate $s(a)$ under different values of α and β.

In the next subsection, the error of the numerical approximation of the model for the two given simulations is analyzed.

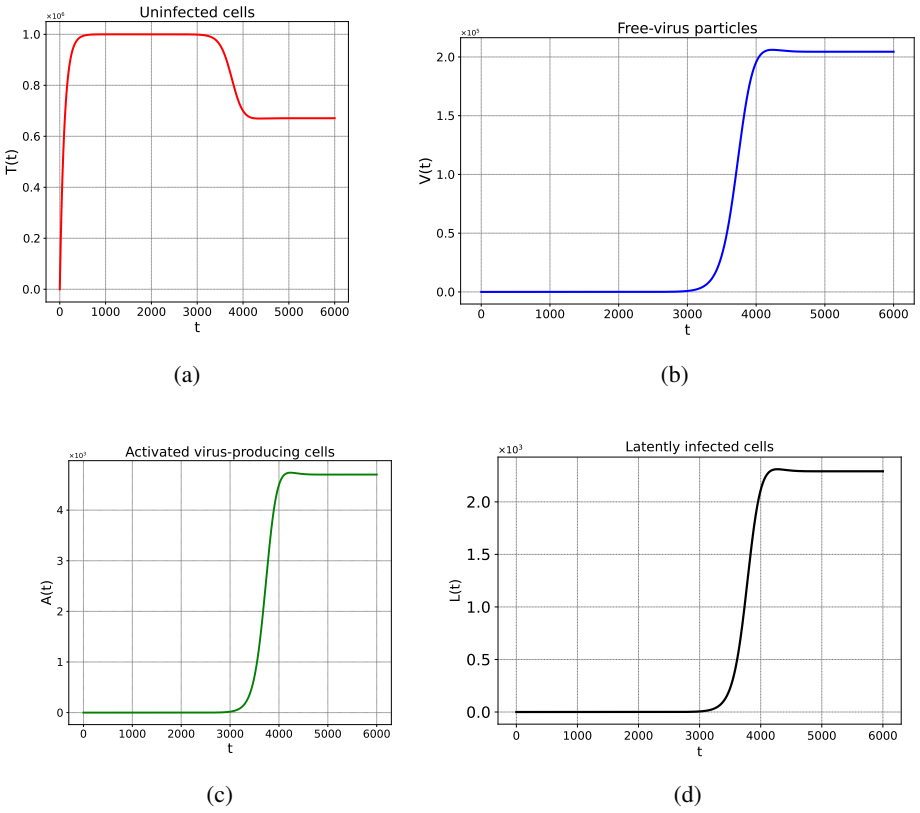

Figure 2. Numerical simulation of the model (1.2) using the transactivation rate defined by a gamma distribution with $\alpha = 8.070335$ and $\beta = 20.289536$ when $R_0 = 1.4906 > 1$. The panels show the time evolution of (a) uninfected cells $T(t)$, (b) free–virus particles $V(t)$, (c) activated virus-producing cells $A(t)$, and (d) latently infected cells $L(t)$.

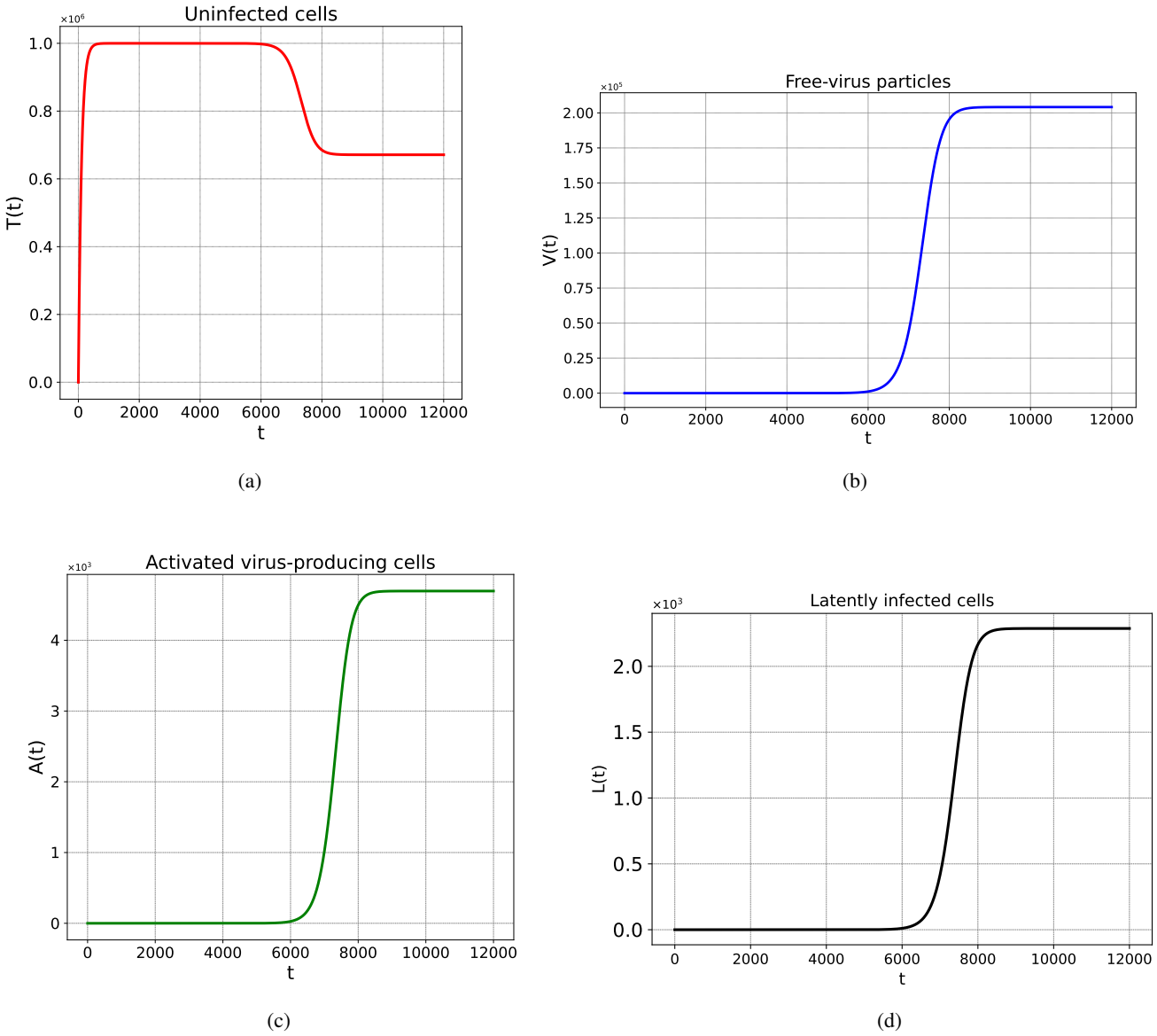

(a) (b) (c) (d)

Figure 3. Numerical solution of the model (1.2) using a transactivation defined by $\alpha = 1.543579$, $\beta = 0.031014$, and $R_0 = 1.4906 > 1$. Panels display the time evolution of (a)–(d) as described in Figure 2.

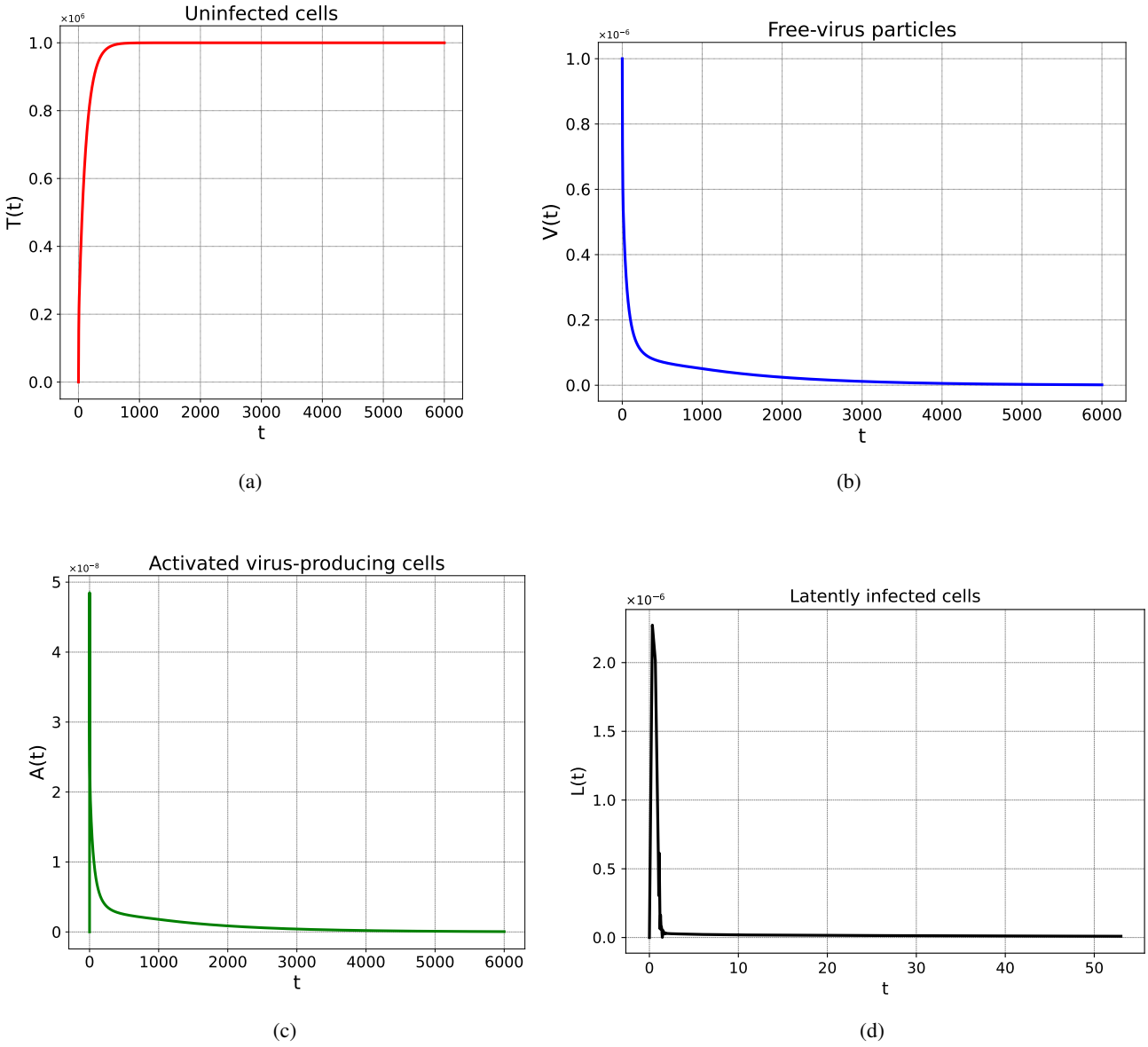

Figure 4. Numerical solution of the model (1.2) with the same transactivation profile as in Figure 2, but when $R_0 = 0.9689 < 1$. Panels (a)–(d) show the same variables as in Figure 2, reflecting the progression toward viral clearance.

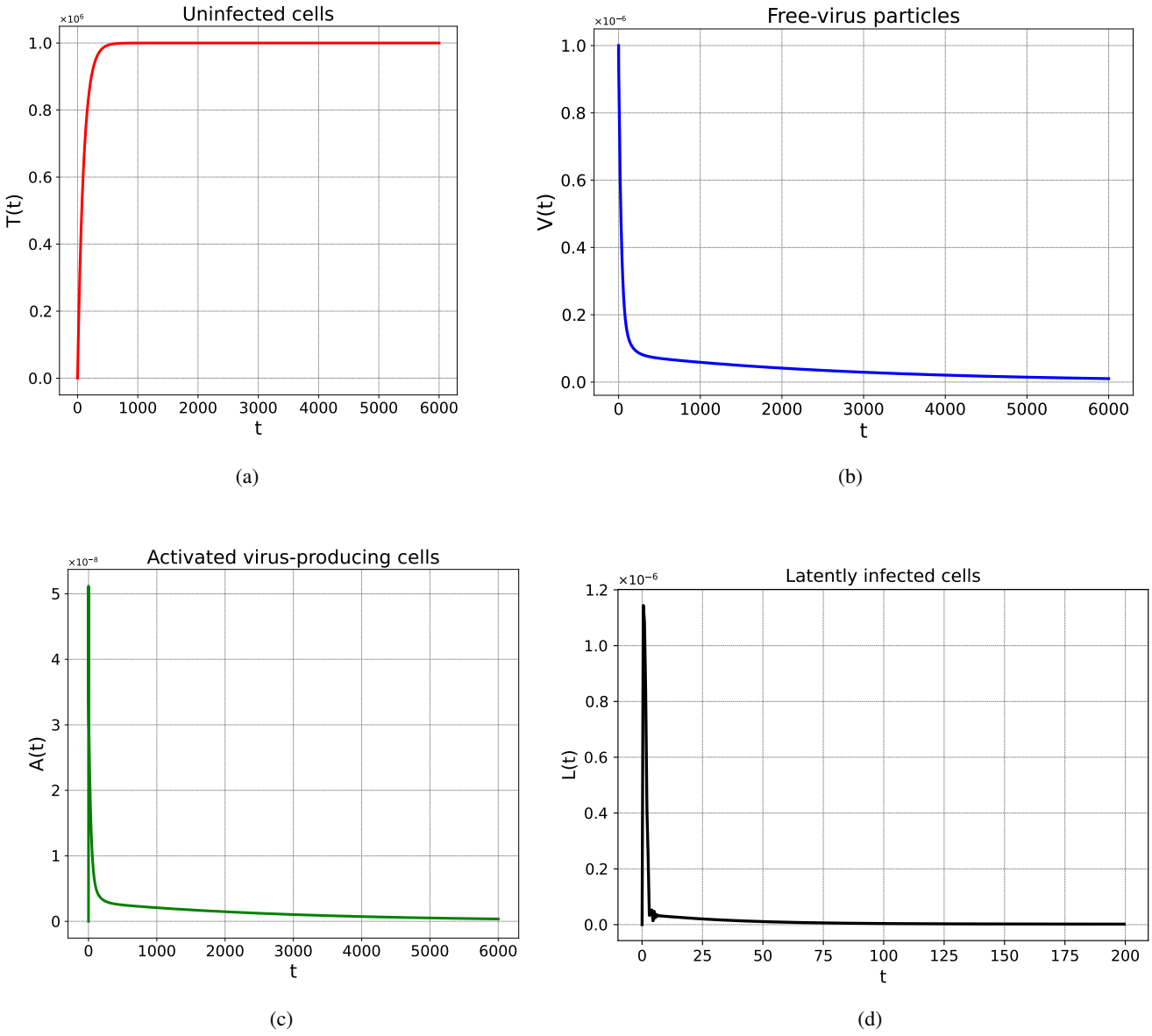

Figure 5. Numerical simulation of the model (1.2) for the same transactivation profile as in Figure 3 when $R_0 = 0.9689 < 1$. The system evolves toward infection clearance.

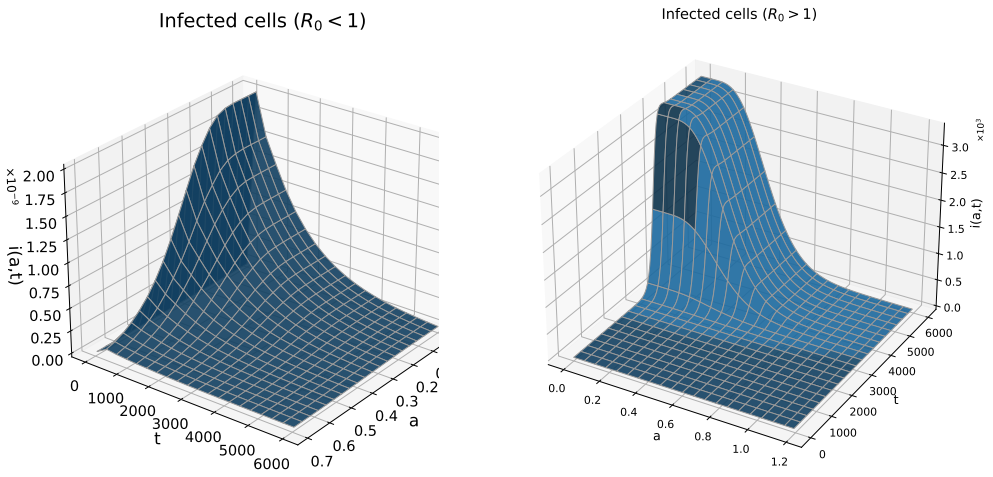

(a) (b)

Figure 6. Evolution of the infected cell $i(a,t)$ when using the gamma distribution with $\alpha = 8.070335$ and $\beta = 20.289536$. Panel (a) corresponds to $R_0 = 0.9689 < 1$ and the virus production rate $p = 650$. Panel (b) shows the case when $R_0 = 1.4906 > 1$ with $p = 1000$, where the infection persists.

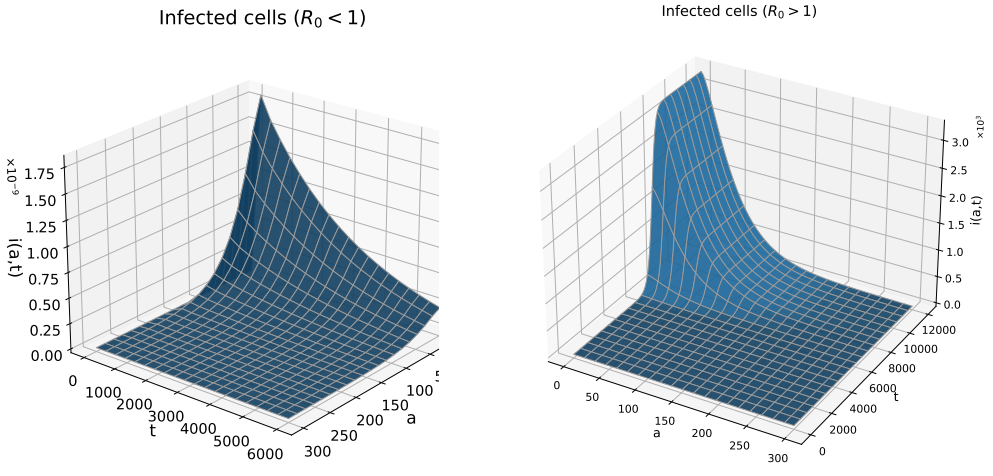

(a) (b)

Figure 7. Evolution of the infected cell $i(a,t)$ with the gamma distribution $\alpha = 1.543579$, $\beta = 0.031014$. Panel (a) shows the case with $R_0 = 0.9689 < 1$ and $p = 650$, while Panel (b) displays the case with $R_0 = 1.4906 > 1$.

3.4.2. Error analysis

Since we do not know the exact solution of the virus dynamics model, we use the equilibria and their stability results to analyze the error due to the numerical approximation of the model. That is, we compare the coordinates of the two equilibrium points E^0 and E^* with the numerical solutions at the last time level t_f ($t \to \infty$). With this information, the numerical deviations can be measured. We consider the absolute error, which is defined by

$$e_{abs} = \begin{cases} \left|u^{\star}_{num}(t^{M+1}) - u^{\star}_{exact}\right|, \\ \left|\mathrm{i}(a_j, t^{M+1}) - i^*(a_j)\right|, \end{cases} \tag{3.12}$$

where $u^{\star}_{num}(t^{M+1})$ represents the numerical approximation of $T(t^{M+1})$, $V(t^{M+1})$, $A(t^{M+1})$, or $L(t^{M+1})$, while $u^{\star}_{exact}$ denotes the coordinates of the positive equilibrium T^*, V^*, A^*, or L^*. The time t^{M+1} is the last time level in the interval $[0, t_f]$. The error due to the approximation of $i(a_j, t^{M+1})$ is evaluated along different values of a_j, comparing these errors and selecting the maximum. Table 2 presents the absolute errors for the infected cells function for both cases of the gamma distribution and R_0, evaluated at the age point where the largest error occurs. This age point can also be visualized in Figure 8.

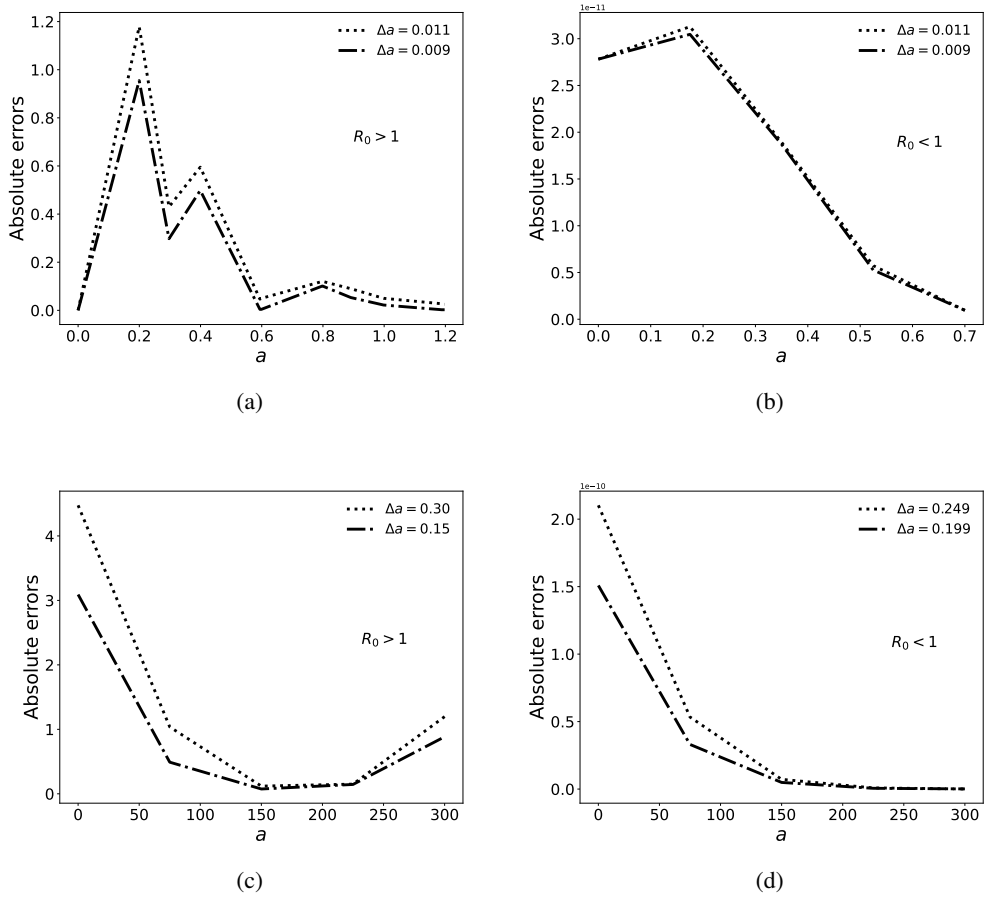

Figure 8. Absolute error of the numerical approximation of infected cells $i(a, t)$ at the final time step t^{M+1} for different values of a. Panels (a) and (b) correspond to $\alpha = 8.070335$ and $\beta = 20.289536$, while Panels (c) and (d) correspond to $\alpha = 1.543579$ and $\beta = 0.031014$.

Table 2. Absolute error and convergence rate of the numerical approximation for $i(a_j, t^{M+1})$, where a_j is the age point where the largest error occurs. The symbol $\star$ refers to the gamma distribution with the parameters $\alpha = 8.070335$ and $\beta = 20.289536$, while $\star\star$ corresponds to $\alpha = 1.543579$ and $\beta = 0.031014$; $\Delta t = 0.399$ is used, except in the last row, where $\Delta t = 0.5$.

Function	Absolute error					
	$\Delta a\star$					
	0.016	0.014	0.012	0.011	0.009	
$i(0.2, t)$	2.516	1.904	1.392	1.178	0.954	$R_0 > 1$
rate	2.084	2.034	1.912	1.050		
$i(0.18, t)$	6.464e-11	4.865e-11	3.676e-11	3.129e-11	3.046e-11	$R_0 < 1$
rate	2.127	1.819	1.851	0.133		
	$\Delta a\star\star$					
	0.599	0.300	0.150	0.075	0.037	
$i(0, t)$	8.346	4.475	3.091	1.660	0.663	$R_0 > 1$
rate	0.901	0.534	0.897	1.299		
	$\Delta a\star\star$					
	0.748	0.375	0.299	0.249	0.199	
$i(0, t)$	2.472e-10	2.457e-10	2.361e-10	2.102e-10	1.508e-10	$R_0 < 1$
rate	0.009	0.177	0.633	1.480		

To analyze the absolute error of the numerical approximations for the functions $T(t)$, $V(t)$, $A(t)$, and $L(t)$, Tables 3 and 4 show the error values when $R_0 > 1$ and $R_0 < 1$, respectively, using the gamma distribution with the parameters $\alpha = 8.070335$ and $\beta = 20.289536$. It should be noted that one of the main factors contributing to the error is the choice of Δa. While Δt also plays a role, it remains fixed in the numerical experiments. From Figures 9(b) and 10(b), it is evident that as $\Delta a \to 0$, the errors decrease, confirming the consistency of the numerical scheme used to solve the PDE [25, 27, 30]. Figures 9(a) and 10(a) highlight notable behaviors in the absolute error. The results indicate that the error decreases gradually and only becomes significant for $\Delta a < 0.249$ (Figure 9(a)), while in Figure 10(a), the errors remain almost constant. In the latter case, to further reduce the error after achieving good accuracy in the age discretization, it is also necessary to reduce the time step Δt to maintain consistency between the age and temporal discretizations. Since the Runge–Kutta and Crank–Nicolson methods are combined, the numerical approximation errors can arise from several factors, primarily truncation and rounding errors [33–35]. Theoretically, the fourth-order Runge–Kutta method has a fourth-order global truncation error, while the Crank–Nicolson method has a second-order error. To analyze how the error changes as Δa and Δt are reduced, we calculate the estimates of the convergence rate by comparing the errors from the simulations. These estimates offer insight into whether the observed convergence rate aligns with the theoretical results or is affected by the lower-order method. The rate is calculated using the following expression:

$$\text{rate} = \frac{\log(\text{error}_1/\text{error}_2)}{\log(\Delta_1/\Delta_2)},$$

where error_1 is the absolute error corresponding to the step size Δ_1 (either age or temporal), while

error$_2$ is the error when the step size is reduced to Δ_2. In Table 2, the convergence rate of the numerical method is included by reducing Δa while keeping Δt fixed at a specific value. In Tables 5 and 6, the rate is calculated by reducing Δt, with Δa fixed at the value given in the last column of Tables 3, 4, 7, and 8.

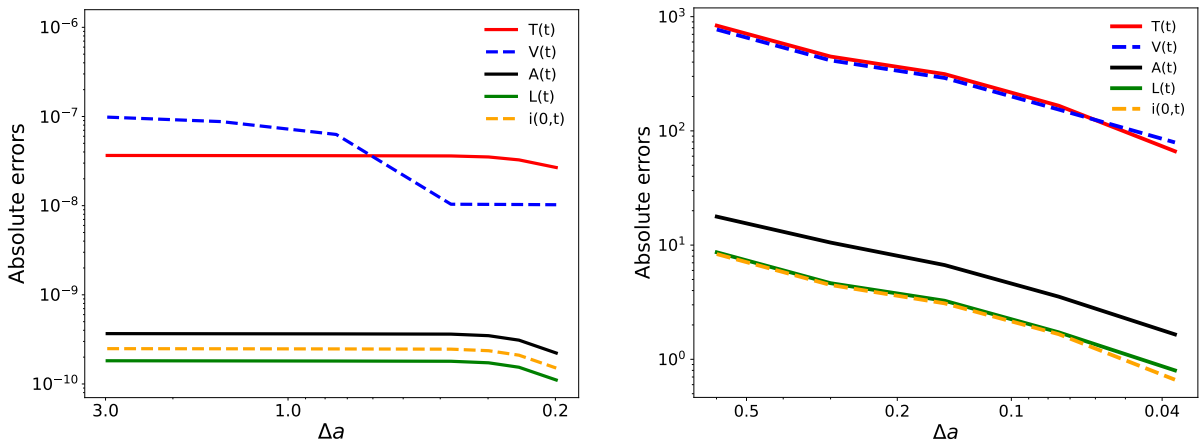

Figure 9. Log-log plot of the absolute error versus the spatial step size Δa, keeping the time step fixed at $\Delta t = 0.5$, with the gamma distribution $\alpha = 1.543579$ and $\beta = 0.031014$. Panel (a) shows the case with $R_0 = 0.9689 < 1$, while Panel (b) shows the case when $R_0 = 1.4906 > 1$.

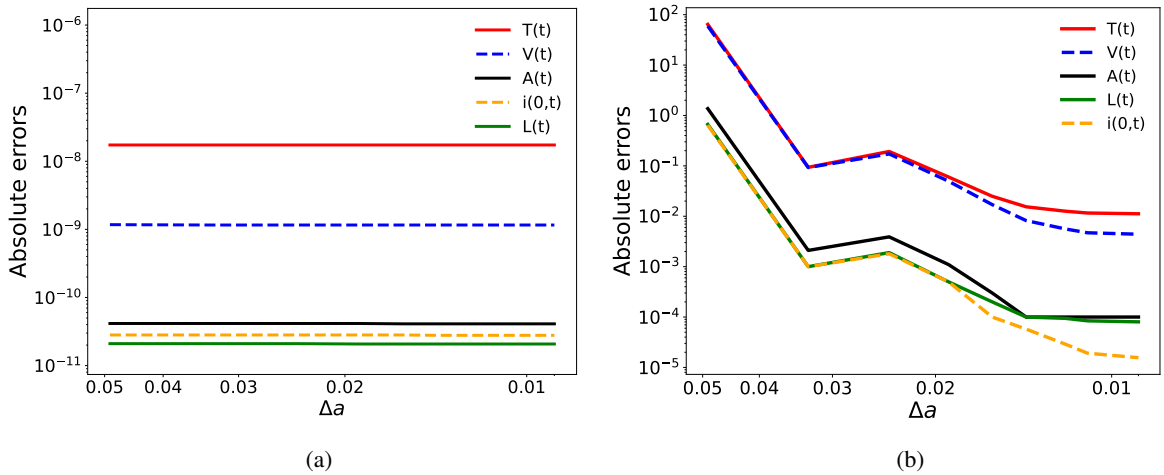

Figure 10. Log-log plot of the absolute error versus the spatial step size Δa, with a fixed $\Delta t = 0.399$, for the gamma distribution with $\alpha = 8.070335$ and $\beta = 20.289536$. Panel (a) illustrates the case with $R_0 = 0.9689 < 1$, and Panel (b) the case when $R_0 = 1.4906 > 1$.

Table 3. Absolute error of the numerical approximation when $R_0 > 1$ and when using the gamma distribution with the parameters $\alpha = 8.070335$ and $\beta = 20.289536$; Δa is varied for a fixed $\Delta t = 0.399$.

Function	Absolute error								
	Δa								
	0.049	0.033	0.024	0.019	0.016	0.014	0.012	0.011	0.009
$T(t)$	64.129	9.35e-2	1.92e-1	6.01e-2	2.49e-2	1.54e-2	1.26e-2	1.16e-2	1.12e-2
$V(t)$	59.377	9.26e-2	1.726e-1	4.96e-2	1.70e-2	8.20e-3	5.60e-3	4.70e-3	4.40e-3
$A(t)$	13.65e-1	2.10e-3	3.90e-3	1.10e-3	3.0e-4	1.0e-4	1.0e-4	1.0e-4	1.0e-4
$L(t)$	6.65e-1	1.0e-3	1.90e-3	5.0e-4	2.0e-4	1.0e-4	9.42e-5	8.41e-5	8.03e-5
$i(0,t)$	6.41e-1	1.0e-3	1.80e-3	5.0e-4	1.0e-4	5.76e-5	2.90e-5	1.92e-5	1.56e-5

Table 4. Absolute error of the numerical approximation when $R_0 < 1$ and when using the gamma distribution with the parameters $\alpha = 8.070335$ and $\beta = 20.289536$; Δa is varied for a fixed $\Delta t = 0.399$.

Function	Absolute error								
	Δa								
	0.049	0.033	0.024	0.019	0.016	0.014	0.012	0.011	0.009
$T(t)$	1.735e-8	1.735e-8	1.735e-8	1.735e-8	1.735e-8	1.735e-8	1.735e-8	1.735e-8	1.735e-8
$V(t)$	1.173e-9	1.159e-9	1.159e-9	1.159e-9	1.159e-9	1.159e-9	1.159e-9	1.159e-9	1.159e-9
$A(t)$	4.151e-11	4.151e-11	4.151e-11	4.151e-11	4.101e-11	4.101e-11	4.101e-11	4.101e-11	4.101e-11
$L(t)$	2.100e-11	2.100e-11	2.100e-11	2.075e-11	2.075e-11	2.075e-11	2.075e-11	2.075e-11	2.075e-11
$i(0,t)$	2.815e-11	2.815e-11	2.815e-11	2.815e-11	2.815e-11	2.781e-11	2.781e-11	2.781e-11	2.781e-11

Table 5. Absolute errors and convergence rates when using the gamma distribution with $\alpha = 8.070335$ and $\beta = 20.289536$, for both cases of R_0. The time step Δt is varied, while $\Delta a = 0.009$ remains fixed.

Δt	$T(t)$	rate	$V(t)$	rate	$A(t)$	rate	$L(t)$	rate
				$R_0 > 1$				
0.399	1.12e-2		4.40e-3		1.00e-4		8.03e-5	
0.333	1.09e-2	0.150	4.20e-3	0.257	9.65e-5	0.193	7.73e-5	0.207
0.285	1.07e-2	0.119	4.00e-3	0.313	9.38e-5	0.174	7.52e-5	0.175
0.249	1.05e-2	0.139	3.90e-3	0.187	9.18e-5	0.168	7.37e-5	0.152
				$R_0 < 1$				
0.399	1.73e-8		1.15e-9		4.10e-11		2.07e-11	
0.333	1.62e-8	0.359	1.11e-9	0.216	3.93e-11	0.222	2.03e-11	0.117
0.285	1.56e-8	0.226	1.08e-9	0.182	3.81e-11	0.206	2.01e-11	0.062
0.249	1.53e-8	0.172	1.06e-9	0.161	3.72e-11	0.185	2.00e-11	0.018

Table 6. Absolute errors and convergence rates when using the gamma distribution with $\alpha = 1.543579$ and $\beta = 0.031014$. The time step Δt is varied, while $\Delta a = 0.037$ is kept fixed for $R_0 > 1$; the errors for $T(t)$ and $V(t)$ are scaled by 10^2, whereas those for $A(t)$ and $L(t)$ are scaled by 10. For $R_0 < 1$, $\Delta a = 0.199$ is fixed.

					$R_0 > 1$			
Δt	$T(t)$	rate	$V(t)$	rate	$A(t)$	rate	$L(t)$	rate
0.399	0.6630		0.7923		0.1652		0.0798	
0.333	0.6034	0.521	0.7655	0.190	0.1404	0.899	0.0655	1.092
0.285	0.5677	0.392	0.7461	0.165	0.1209	0.961	0.0532	1.336
0.249	0.5421	0.342	0.7303	0.159	0.1045	1.079	0.0422	1.715
					$R_0 < 1$			
0.500	2.677e-8		1.023e-8		2.224e-10		1.108e-10	
0.399	2.583e-8	0.159	1.004e-8	0.085	2.176e-10	0.096	1.039e-10	0.284
0.333	2.560e-8	0.049	0.992e-8	0.068	2.156e-10	0.053	1.019e-10	0.106
0.285	2.543e-8	0.043	0.990e-8	0.010	2.146e-10	0.029	0.999e-10	0.128

Table 7. Absolute error of the numerical approximation when $R_0 > 1$ and when using the gamma distribution with the parameters $\alpha = 1.543579$ and $\beta = 0.031014$; Δa is varied for a fixed $\Delta t = 0.399$. The errors for $T(t)$ and $V(t)$ are scaled by 10^2, whereas those for $A(t)$, $L(t)$, and $i(0, t)$ are scaled by 10.

Function	Absolute error				
			Δa		
	0.599	0.300	0.150	0.075	0.037
$T(t)$	8.3463	4.4749	3.1406	1.6604	0.6630
$V(t)$	7.7182	4.1405	2.9065	1.5377	0.7923
$A(t)$	1.7751	1.0523	0.6684	0.3537	0.1652
$L(t)$	0.8648	0.4639	0.3256	0.1723	0.0798
$i(0, t)$	0.8346	0.4475	0.3091	0.1660	0.0663

Table 8. Absolute error of the numerical approximation when $R_0 < 1$ and when using the gamma distribution with the parameters $\alpha = 1.543579$ and $\beta = 0.031014$; Δa is varied for a fixed $\Delta t = 0.5$.

Function	Absolute error						
				Δa			
	2.970	1.493	0.748	0.375	0.299	0.249	0.199
$T(t)$	3.655e-8	3.644e-8	3.632e-8	3.611e-8	3.516e-8	3.260e-8	2.678e-8
$V(t)$	9.837e-8	8.761e-8	6.287e-8	1.037e-8	1.033e-8	1.030e-8	1.024e-8
$A(t)$	3.671e-10	3.658e-10	3.645e-10	3.623e-10	3.481e-10	3.100e-10	2.225e-10
$L(t)$	1.821e-10	1.815e-10	1.808e-10	1.797e-10	1.727e-10	1.540e-10	1.108e-10
$i(0, t)$	2.490e-10	2.482e-10	2.472e-10	2.457e-10	2.361e-10	2.103e-10	1.509e-10

The convergence rate values in Table 2 clearly indicate that the error decreases slowly. Since Δt remains relatively large, the temporal error dominates the numerical solution, limiting the overall convergence rate. Theoretically, the rate should be close to 2, given the use of the Crank–Nicolson method; however, the values converge to the expected rate as Δt is further reduced. Nevertheless, when both methods are combined, the overall error may be governed by the lower-order component, leading to a slower rate of error reduction [25, 36].

On the other hand, by reducing Δt, the temporal discretization error decreases; however, if the error in the age variable remains large, the reduction in the total error will be minimal. Tables 5 and 6 present the convergence rates as Δt is reduced. From these results, the observed rates are significantly lower than the theoretical expectation, suggesting that the error in the age variable dominates the total error. To achieve a more substantial decrease in error and a convergence rate closer to the theoretical one, it is advisable to balance both step sizes. Given the high computational cost, we have limited ourselves to the results obtained.

In Tables 7 and 8, errors are given for when utilizing the gamma distribution with $\alpha = 1.543579$ and $\beta = 0.031014$. In this scenario, the approximations for $R_0 > 1$ require Δa to be sufficiently small. For the purpose of visualizing the model's solution, the graphs were generated with $\Delta a = 0.037$, resulting in a prolonged running time of 111.92 hrs (4.66 days); see Figure 11. Opting for an even smaller Δa is favorable for enhanced precision, but it comes at the cost of increased computation time.

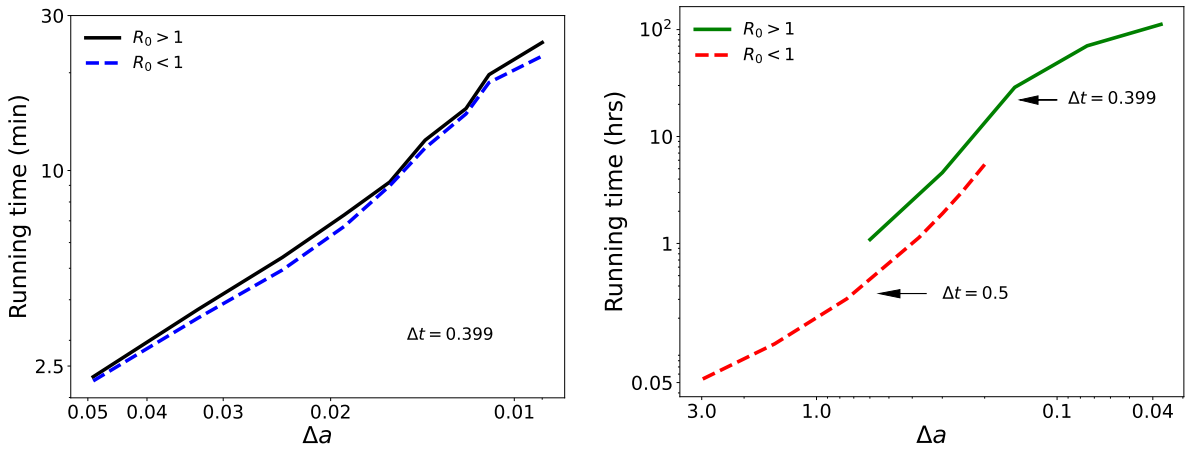

(a) (b)

Figure 11. Log-log plot of the running times for the numerical solution of the model (1.2). (a) Transactivation rate using a gamma distribution with $\alpha = 8.070335$ and $\beta = 20.289536$. (b) Gamma distribution with $\alpha = 1.543579$ and $\beta = 0.031014$.

The approximations for $R_0 < 1$ resulted in using a larger Δt and Δa than the previous case. In this case, the running time for the last column of Table 8 was only 5.54 hr, resulting in errors of the order of 10^{-8} and 10^{-10}.

We analyze the behavior of the absolute error for the approximation of the infected cells at the final time level t^{M+1} and for different values of a_j. The range of values a_j depends on the gamma distribution parameters α and β used, as shown in Figures 6 and 7. Due to the high computational cost required

for obtaining numerical solutions of the model, we calculate the absolute error for only a few values of a. Figure 8 shows the absolute error in the approximation of $i(a,t)$ for both $R_0 > 1$ and $R_0 < 1$. A decrease in error as Δa is reduced is observed, which is consistent with expectations.

Figure 8(a) illustrates the behavior of the absolute error when $R_0 > 1$, with $\alpha = 8.070335$ and $\beta = 20.289536$, using a time step size of $\Delta t = 0.399$ and varying the age step size Δa. The figure shows that at certain specific ages, the error is significantly higher compared with other values of a, indicating potential challenges in accurately computing the solution in these regions of the domain. Conversely, when $R_0 < 1$, the error decreases more gradually. In Figure 8(b), the error decreases as the age increases, suggesting that the numerical solution is more accurate at these values of a.

Figure 8(c) corresponds to the case where $R_0 > 1$, with $\alpha = 1.543579$ and $\beta = 0.031014$, using $\Delta t = 0.399$. The choice of Δa was made by considering the computational time required to obtain the solutions, making this case the most resource-intensive. This plot reveals challenges across different age ranges, suggesting that further mesh refinement may be necessary to improve accuracy. In Figure 8(d), where $R_0 < 1$ and $\Delta t = 0.5$, the error consistently decreases as age increases, indicating that the solution effectively captures the dynamics of $i(a,t)$ as the cells age. Notably, although the error at $a = 0$ is the highest (1.5088×10^{-10}), it remains low, demonstrating that the numerical scheme is accurate even in at early ages.

4. Sensitivity of the model parameters

4.1. Global sensitivity analysis

In order to identify the parameters that most influence the model's dynamics, this section performs a global sensitivity analysis. We focus on the case with $R_0 > 1$, as this is when the model exhibits persistent infection dynamics. This analysis consisted of systematically varying each key model parameter, both above and below its fixed value (see Table 1 for the reference values), thereby observing changes in the model's dynamics results (see Figure 12). In particular, the behavior of $T(t)$, $V(t)$, $L(t)$, and $A(t)$ is observed. For each key parameter, a range of values that varied around a reference value was selected, while keeping the other parameters fixed. This allows the impact of each parameter on the numerical solution of the model to be identified.

The results of the sensitivity analysis show the following.

When $R_0 > 1$, from Figure 12, as the value of λ decreases, the number of new infections also decreases, which means that fewer cells are infected; therefore, the number of activated cells $A(t)$ decreases. On the other hand, virus production decreases, meaning that $V(t)$ takes a lower value. Relative to $L(t)$, it reduces the transition to the latent state. The increase in $T(t)$ confirms that reducing the infection rate λ is an effective strategy for preserving the healthy cell population.

Decreasing the values of p and ψ shows that $V(t)$, $A(t)$, and $L(t)$ acquire lower values compared with the solutions obtained using the fixed reference values. This dynamic reflects lower virus production and spread within the system; that is, the decrease in p means that each activated cell releases fewer viruses, reducing the system's infectious capacity and feedback loop. Additionally, a smaller number of healthy cells that can enter the system reduces the susceptible population that can be infected.

With respect to γ, c, and δ, decreasing their values shows that $V(t)$, $A(t)$, and $L(t)$ increase in value, indicating greater persistence of the virus in the system. A lower γ rate prolongs the lifespan of uninfected cells. Reducing δ decreases the elimination of activated cells. Likewise, a lower value of

the c rate reduces the clearance of viral particles. These behaviors align with what has already been reported in previous studies [2, 4, 37].

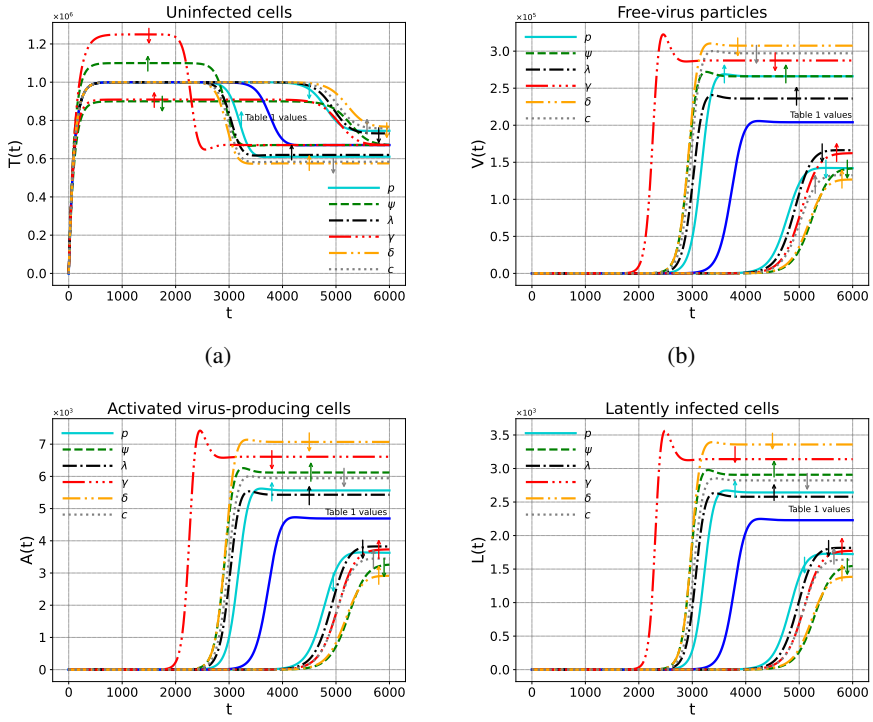

Figure 12. Global sensitivity analysis of the model's dynamics with respect to some of its parameters when $R_0 > 1$. The blue line represents the solution corresponding to the reference values indicated in Table 1. In (a)–(d), the upward arrows indicate an increase in the parameter's value with respect to the reference values, while the downward arrows represent a decrease.

4.2. Local sensitivity analysis

We conducted a local sensitivity analysis to evaluate the influence of key parameters on the basic reproductive number, R_0, with a particular focus on classic control parameters in viral infections (λ, p, c, and γ), as well as the per-cell death rate of activated infected cells (δ), the reversion rate of activated infected cells to latently infected cells (r), and the activation rate of latently infected cells to activated infected cells (η). The sensitivity index quantifies how a fractional change in a parameter affects a fractional change in R_0, assuming that all other parameters remain constant. It is defined as $E_\tau = \frac{\tau}{R_0}\frac{\partial R_0}{\partial \tau}$, where τ represents the parameter under evaluation [38]. We calculated the sensitivity indices for several parameters

$$E_\lambda = E_p = -E_c = -E_\gamma = 1,$$

$$E_\eta = \frac{r\mu\eta}{(\eta+\mu)(\delta\eta+\mu(r+\delta))},$$

$$E_r = -\frac{r\mu}{\delta\eta+\mu(r+\delta)},$$

$$E_\delta = -\frac{\delta(\eta+\mu)}{\delta\eta+\mu(r+\delta)}.$$

The sensitivity indices show that the parameters λ, p, and η have a direct relationship with R_0, while c, γ, δ, and r have an inverse relationship with R_0. We interpret the negative relationship between r and R_0 as follows: Increasing the reversion rate of activated infected cells to latently infected cells leads to a decrease in R_0. In other words, shortening the reversion period $(1/r)$ results in a lower R_0. A similar interpretation can be given for the negative relationship between the per-cell death rate of activated infected cells (δ) and R_0. Additionally, the positive relationship between η and R_0 suggests that decreasing the activation rate of latently infected cells to activated infected cells reduces R_0. We have used the fixed values of Table 1 and obtained: $E_\eta = 6.6116 \times 10^{-4}$, $E_r = -6.7811 \times 10^{-4}$, and $E_\delta = -9.9993 \times 10^{-1}$. These numerical results indicate that η and r play a minor role in the control of the infection.

5. Discussion

The global stability of the basic age-dependent viral infection model without latent cells [9, 10] has been fully characterized [14], as well as that of age-structured models with two cell populations [23]. Moreover, ODE models including latent cells have been extensively studied in terms of their solutions [5, 40]. The model analyzed in this work introduces two aspects: A age-dependent transactivation rate and the inclusion of a latent cell population [15]. From a qualitative perspective, the numerical simulations also confirm the theoretical results regarding the global asymptotic behavior of the model. Specifically, the present simulations preserve the characteristics of positivity and boundedness for $T(t)$, $i(a,t)$, $A(t)$, $L(t)$, and $V(t)$. With $R_0 < 1$, the system transitions toward virus-free equilibrium, aligning with the notion that the infection disappears. Conversely, for $R_0 > 1$, the infected equilibrium emerges as a globally stable attractor, meaning that the infection persists.

On the other hand, in the quantitative part, the choice of the discretization steps Δt (time) and Δa (age) significantly influences both the accuracy and stability of the numerical solution. An excessively long Δa results in numerical instability in the solution. Conversely, when this step size is refined too much, the computational cost increases substantially, since a finer Δa requires more iterations to solve the entire domain. We performed additional numerical experiments (see Tables 2–8) that revealed that refining Δa improves the accuracy of the numerical solution.

Furthermore, to solve the hyperbolic PDE using the Crank–Nicolson method, the stability was experimentally analyzed, confirming that the time mesh must be larger than the age mesh. If Δt becomes significantly smaller than Δa, spurious solutions may arise. Overall, these findings highlight the need to balance step size selection with high computational demands. By properly combining a Δa with a time step Δt, we achieve adequate stability and accuracy, as demonstrated in the error and convergence analyses (Sections 3.4.1 and 3.4.2) and in the reported running times (Figure 11).

Sensitivity analysis, both local and global, provides valuable information for identifying potential strategies to control a viral infection. The results of the local sensitivity analysis should be interpreted in conjunction with the simulated outputs of the viral dynamics models from the global analysis, as well as the potential interventions. Classically, it has been shown that the dynamics of HIV-1 infection can be controlled through antiretroviral therapies, which are designed to inhibit both new infections and viral replication. These therapies target key parameters such as the viral transmission rate (λ)

and the viral production rate (p). The viral clearance rate (c) could be increased by the antibody immune response induced by vaccines. Recently, a clinical proof of concept (NCT03547245) has been established for boosting strategies aimed at eliciting broadly neutralizing antibody (bnAb) responses against HIV, providing a potential approach to combat viruses with high antigenic diversity, such as HIV [39]. The death rate of activated infected cells (δ) could be increased by vaccines designed to induce T cell immune responses that are broad, potent, and long-lasting. A recent study shows that early administration of the MF59-adjuvanted Env protein in parallel with DNA priming in macaques leads to modest antibody-dependent cellular cytotoxicity (ADCC) and moderate neutralizing activity. Furthermore, late booster doses contribute to the sustained maintenance of both B and T cell immune responses [41]. These new findings in vaccine design are promising for the control of HIV-1 infection.

6. Conclusions

We analyzed the long-term behavior of an HIV-1 infection model proposed in [15], which accounts for variations in the transactivation rate of recently infected cells proposed in [15]. The model considers the age of infection, a, which keeps track of the time that has passed since the infection of the cell. Age of infection plays a key role in the transactivation rate.

We provided a detailed global stability analysis of the virus-free and infected equilibrium of the age-structured model using the technology of Volterra-type Lyapunov functionals developed in recent papers [11–14, 23], with the infected equilibrium arising by a forward bifurcation.

We fit a gamma distribution to define the age-dependent transactivation rate $s(a)$ using the simulations of Althaus and De Boer [15]. We obtained two sets of parameters from the gamma distribution to perform the numerical simulations.

From the results presented, the expected behaviors of the numerical solution of the model (1.2) were obtained. In all graphs, the solutions are bounded for $t \geq 0$. When $t \to \infty$, these stabilize at the value of the infected equilibrium coordinates E^* or at those of the virus-free equilibrium E^0, depending on the case. On the other hand, from the computational point of view, when $R_0 > 1$, the numerical computation time in both simulations is greater compared with the case when $R_0 < 1$. A critical scenario with a high computational cost arises when α (the shape parameter) and β (the inverse scale parameter) tend to zero in the gamma distribution that appears in the age-dependent transactivation rate $s(a)$. The results of the numerical simulation allowed us to visualize how transactivation profiles influence the distribution of infected cells over time and age. This provides information on how the stages of infection manifest under various biological conditions. These findings highlight the importance of incorporating the age variable into different models of viral dynamics. On the other hand, it is worth mentioning that the absolute error in the two simulations approaches zero as $\Delta a \to 0$. A smaller step size Δt could have been considered, but with the values indicated in Tables 3, 4, and 8, it was sufficient to achieve significant accuracy in the solutions. It is important to highlight that obtaining graphs similar to those in Figure 3 with greater precision, it is required to use both sufficiently small age and time step sizes (see Table 7), but the disadvantage is the high computational cost required.

We have provided a complete classification of the global dynamics of the age-structured model. Possible strategies for controlling viral infections have been identified through a sensitivity analysis. In particular, recent HIV vaccine proposals, designed to induce both B–cell and T–cell immune responses, emerge as a promising approach for effective control.

Author contributions

L.X. Vivas-Cruz: Conceptualization, methodology, investigation, formal analysis, visualization, writing – original draft, writing – review and editing. C. Martínez-Lázaro: Formal analysis, investigation, validation, visualization, writing – original draft, writing – review and editing. C. Vargas-De-León: Conceptualization, methodology, investigation, formal analysis, supervision, funding acquisition, project administration, writing – original draft, writing – review and Editing. All authors have agreed to and given their consent for the publication of this research paper.

Use of Generative–AI tools declaration

The authors declare they have not used artificial intelligence (AI) tools in the creation of this article.

Acknowledgments

This work has been partially supported by the CONAHCYT-Ciencia de Frontera "Ecuaciones de evolución, sus estados estacionarios y su comportamiento asintótico con aplicaciones en Física y Biología" (project No. 684340).

Conflict of interest

The authors declare that they have no conflicts of interest regarding the publication of this manuscript.

References

1. N. Bacaër, *A short history of mathematical population dynamics*, London: Springer, **618** (2011), 89–96. https://doi.org/10.1007/978-0-85729-115-8
2. M. A. Nowak, R. M. May, *Virus dynamics: mathematical principles of immunology and virology*, New York: Oxford University Press, 2000.
3. A. S. Perelson, Modelling viral and immune system dynamics, *Nat. Rev. Immunol.*, **2** (2002), 28–36. https://doi.org/10.1038/nri700
4. A. S. Perelson, P. W. Nelson, Mathematical analysis of HIV-I dynamics in vivo, *SIAM Rev.*, **41** (1999), 3–44. https://doi.org/10.1137/S00361445983351
5. D. S. Callaway, A. S. Perelson, HIV-1 infection and low steady state viral loads, *Bull. Math. Biol.*, **64** (2002), 29–64. https://doi.org/10.1006/bulm.2001.0266
6. W. O. Kermack, A. G. McKendrick, Contributions to the mathematical theory of epidemics. II.—The problem of endemicity, *Proc. R. Soc. Lond. A*, **138** (1932), 55–83. https://doi.org/10.1098/rspa.1932.0171
7. R. M. Anderson, G. F. Medley, R. M. May, A. M. Johnson, A preliminary study of the transmission dynamics of the human immunodeficiency virus (HIV), the causative agent of AIDS, *IMA J. Math. Appl. Med. Biol.*, **3** (1986), 229–263. https://doi.org/10.1093/imammb/3.4.229
8. D. Kirschner, Using mathematics to understand HIV immune dynamics, *Notices AMS*, **43** (1996), 191–202.

9. P. W. Nelson, M. A. Gilchrist, D. Coombs, J. M. Hyman, A. S. Perelson, An age-structured model of HIV infection that allows for variations in the production rate of viral particles and the death rate of productively infected cells, *Math. Biosci. Eng.*, **1** (2004), 267–288. https://doi.org/10.3934/mbe.2004.1.267
10. L. Rong, Z. Feng, A. S. Perelson, Mathematical analysis of age-structured HIV-1 dynamics with combination antiretroviral therapy, *SIAM J. Appl. Math.*, **67** (2007), 731–756. https://doi.org/10.1137/060663945
11. P. Magal, C. C. McCluskey, G. F. Webb, Lyapunov functional and global asymptotic stability for an infection-age model, *Appl. Anal.*, **89** (2010), 1109–1140. https://doi.org/10.1080/00036810903208122
12. C. C. McCluskey, Delay versus age-of-infection-global stability, *Appl. Math. Comput.*, **217** (2010), 3046–3049. https://doi.org/10.1016/j.amc.2010.08.037
13. A. V. Melnik, A. Korobeinikov, Lyapunov functions and global stability for SIR and SEIR models with age-dependent susceptibility, *Math. Biosci. Eng.*, **10** (2013), 369–378. https://doi.org/10.3934/mbe.2013.10.369
14. G. Huang, X. Liu, Y. Takeuchi, Lyapunov functions and global stability for age-structured HIV infection model, *SIAM J. Appl. Math*, **72** (2012), 25–38. https://doi.org/10.1137/110826588
15. C. L. Althaus, R. J. De Boer, Intracellular transactivation of HIV can account for the decelerating decay of virus load during drug therapy, *Mol. Syst. Biol.*, **6** (2010), 348. https://doi.org/10.1038/msb.2010.4
16. M. S. Arif, K. Abodayeh, Y. Nawaz, Construction of a computational scheme for the fuzzy HIV/AIDS epidemic model with a nonlinear saturated incidence rate, *Comput. Model. Eng. Sci.*, **138** (2024), 145–1425. https://doi.org/10.32604/cmes.2023.028946
17. M. S. Arif, K. Abodayeh, Y. Nawaz, A hybrid SIR-fuzzy model for epidemic dynamics: a numerical study, *Comput. Model. Eng. Sci.*, **139** (2024), 3417–3434. https://doi.org/10.32604/cmes.2024.046944
18. G. Webb, *Theory of nonlinear age-dependent population dynamics*, CRC Press, 1985.
19. J. A. J. Metz, O. Diekmann, *The dynamics of physiologically structured populations*, Springer, **68** (1986). https://doi.org/10.1007/978-3-662-13159-6
20. L. M. Abia, O. Angulo, J. C. López-Marcos, Age-structured population models and their numerical solution, *Ecol. Model.*, **188** (2005), 112–136. https://doi.org/10.1016/j.ecolmodel.2005.05.007
21. Y. Kuang, *Delay differential equations*, New York: Academic press, 1993.
22. R. J. H. Payne, M. A. Nowak, B. S. Blumberg, Analysis of a cellular model to account for the natural history of infection by the hepatitis B virus and its role in the development of primary hepatocellular carcinoma, *J. Theor. Biol.*, **159** (1992), 215–240. https://doi.org/10.1016/S0022-5193(05)80703-9
23. P. Wu, H. Zhao, Mathematical analysis of multi-target cells and multi-strain age-structured model with two HIV infection routes, *Int. J. Biomath.*, **14** (2021), 2150057. https://doi.org/10.1142/S1793524521500571
24. G. D. Smith, *Numerical solution of partial differential equations: finite difference methods*, 3Eds., Clarendon Press, 1986

25. R. J. LeVeque, *Finite difference methods for ordinary and partial differential equations: steady-state and time-dependent problems*, SIAM, 2007.

26. K. W. Morton, D. F. Mayers, *Numerical solution of partial differential equations: an introduction*, 2 Eds., Cambridge University Press, 2012. https://doi.org/10.1017/CBO9780511812248

27. J. Crank, P. Nicolson, A practical method for numerical evaluation of solutions of partial differential equations of the heat-conduction type, *Adv. Comput. Math.*, **6** (1996), 207–226. https://doi.org/10.1007/BF02127704

28. E. Hairer, M. Roche, C. Lubich, *The numerical solution of differential-algebraic systems by Runge-Kutta methods*, Springer, 1989. https://doi.org/10.1007/BFb0093947

29. J. C. Butcher, *Numerical methods for ordinary differential equations*, John Wiley & Sons, 2016. https://doi.org/10.1002/9781119121534

30. P. D. Lax, R. D. Richtmyer, Survey of the stability of linear finite difference equations, *Commun. Pure Appl. Math.*, **9** (1956), 267–293.

31. J. C. Strikwerda, *Finite difference schemes and partial differential equations*, SIAM, 2004.

32. H. K. Rouf, F. Costen, S. G. Garcia, 3D Crank-Nicolson finite difference time domain method for dispersive media, *Electron. Lett.*, **45** (2009), 961–962. https://doi.org/10.1049/el.2009.1940

33. J. Stoer, R. Bulirsch, *Introduction to numerical analysis*, New York: Springer, 1993. https://doi.org/10.1007/978-1-4757-2272-7

34. N. J. Higham, *Accuracy and stability of numerical algorithms*, SIAM, 2002.

35. A. Quarteroni, R. Sacco, F. Saleri, *Numerical mathematics*, Springer Science & Business Media, 2006.

36. A. Ostermann, M. Roche, Runge-Kutta methods for partial differential equations and fractional orders of convergence, *Math. Comp.*, **59** (1992), 403–420. https://doi.org/10.1090/S0025-5718-1992-1142285-6

37. M. Martcheva, *An introduction to mathematical epidemiology*, New York: Springer, 2015. https://doi.org/10.1007/978-1-4899-7612-3

38. A. L. Lloyd, Sensitivity of model-based epidemiological parameter estimation to model assumptions, In: *Mathematical and statistical estimation approaches in epidemiology*, Springer, 2009, 123–141. https://doi.org/10.1007/978-90-481-2313-1_6

39. D. J. Leggat, K. W. Cohen, J. R. Willis, W. J. Fulp, A. C. Decamp, O. Kalyuzhniy, et al., Vaccination induces HIV broadly neutralizing antibody precursors in humans, *Science*, **378** (2022), eadd6502. https://doi.org/10.1126/science.add6502

40. B. Buonomo, C. Vargas-De-León, Global stability for an HIV-1 infection model including an eclipse stage of infected cells, *J. Math. Anal. Appl.*, **385** (2012), 709–720. https://doi.org/10.1016/j.jmaa.2011.07.006

41. B. Perdiguero, B. Asbach, C. E. Gómez, J. Köstler, S. W. Barnett, M. Koutsoukos, et al., Early and long-term HIV-1 immunogenicity induced in macaques by the combined administration of DNA, NYVAC, and Env protein-based vaccine candidates: the AUP512 study, *Front. Immunol.*, **13** (2022), 939627. https://doi.org/10.3389/fimmu.2022.939627

Appendix

Pseudocode for the simulations of the age-structured HIV model.

Algorithm 1 Pseudocode

Input: Parameters $\psi, \gamma, \lambda, r, \eta, \delta, \mu, p, c$ ▷ Model parameter values
Input: Initial conditions $T_0,\ V_0,\ A_0,\ L_0,\ i_0(a)$ ▷ Initial conditons of the model
Input: Grid parameters (a_I, a_F, N) and (t_I, t_F, M) ▷ $a_I = 0$, $t_I = 0$
▷ a_F is a sufficiently large number for numerical purposes.

1. Allocate arrays
Allocate vectors $\mathbf{t}[0..M+1]$, $\mathbf{a}[0..N+1]$ ▷ To store time and age
Allocate vectors $\mathbf{T}[0..M+1]$, $\mathbf{V}[0..M+1]$, $\mathbf{A}[0..M+1]$, $\mathbf{L}[0..M+1]$ ▷ To variables T, V, A, L
Allocate matrix $\mathbf{M}[(M+2)\times(N+2)]$ ▷ To store $i(a_j, t^k)$

2. Discretize age and time grids
$a_j \leftarrow a_I + j\,\Delta a,\quad j = 0, \ldots, N+1$ ▷ $\Delta a = a_F/(N+1)$
$t^k \leftarrow t_I + k\,\Delta t,\quad k = 0, \ldots, M+1$ ▷ $\Delta t = t_F/(M+1)$

3. Define initial and boundary condition function for $i(a,t)$
$\mathsf{IC}(a) \leftarrow 0$ ▷ $i(a,0) = 0$
$\mathsf{BCR}(t) \leftarrow 0$ ▷ $i(a \to \infty, t) = 0$

4. Assign initial and boundary conditions
$\mathbf{T}[0] \leftarrow T_0,\ \mathbf{V}[0] \leftarrow V_0,\ \mathbf{A}[0] \leftarrow A_0,\ \mathbf{L}[0] \leftarrow L_0$
$\mathbf{M}[0,0] \leftarrow \lambda \mathbf{T}[0]\mathbf{V}[0]$ ▷ Initial condition at a_0, $i_0(a_0)$
$\mathbf{M}[0,j] \leftarrow \mathsf{IC}(a_j),\quad j = 1, \ldots, N+1$ ▷ $i(a_j, t^0) = \mathsf{IC}(a_j)$
$\mathbf{M}[k, N+1] \leftarrow \mathsf{BCR}(t^k),\quad k = 1, \ldots, M+1$ ▷ $i(a_{N+1}, t^k) = \mathsf{BCR}(t^k)$

5. Define the function for the transactivation rate
function $\widehat{s}(a;\alpha,\beta)$
  return $\beta^\alpha a^{\alpha-1}\exp(-\beta a)/\Gamma(\alpha)$ ▷ Gamma distribution
end function
function $s(a)$
  return $\widehat{s}(a;\alpha,\beta)/[1 - \int_0^a \widehat{s}(\tau;\alpha,\beta)\,d\tau]$ ▷ Transactivation rate $s(a)$
end function

6. Calculation of the basic reproduction number R_0
function $\rho(a)$
  return $\exp(-\int_0^a s(\phi)\,d\phi)$
end function
Compute $\sigma \leftarrow \int_0^{+\infty} s(a)\,\rho(a)\,da$
Compute $R_0 \leftarrow \dfrac{\psi\, p\, \sigma\, \lambda\, (\eta+\mu)}{\gamma\, c[(\eta+\mu)(r+\delta) - \eta r]}$ ▷ Value of R_0

7. Matrix from the Crank–Nicolson method
$\zeta \leftarrow \Delta t/(4\Delta a)$
$\mathtt{M}_{\mathrm{CN}} \leftarrow \mathrm{tridiag}(-\zeta,\ 1 + \frac{\Delta t}{2} s(a_j),\ \zeta),\quad j = 1, \ldots, N$ ▷ Assembles the tridiagonal matrix

Algorithm 1 Pseudocode (continued)

8. Compute stage slopes $\{g_j^k, m_j^k, w_j^k, \phi_j^k\}_{j=1}^4$ **(Eq** (3.7)**) for the Runge–Kutta method**

$f_1(t^k, T^k, V^k) := \psi - \gamma T^k - \lambda T^k V^k$ ▷ Eq (3.8)

$f_2(t^k, A^k, L^k) := integral - rA^k + \eta L^k - \delta A^k$ ▷ Eq (3.9)

$f_3(t^k, A^k, L^k) := rA^k - \eta L^k - \mu L^k$ ▷ Eq (3.10)

$f_4(t^k, V^k, A^k) := pA^k - cV^k$ ▷ Eq (3.11)

$g_j^k \leftarrow f_1(\mathbf{t}[k] + c_j\Delta t, \mathbf{T}[k] + d_j\Delta t g_{j-1}^k, \mathbf{V}[k] + d_j\Delta t m_{j-1}^k)$ ▷ $k = 1, \ldots, M+1$

$m_j^k \leftarrow f_2(\mathbf{t}[k] + c_j\Delta t, \mathbf{A}[k] + d_j\Delta t w_{j-1}^k, \mathbf{L}[k] + d_j\Delta t \phi_{j-1}^k)$

$w_j^k \leftarrow f_3(\mathbf{t}[k] + c_j\Delta t, \mathbf{A}[k] + d_j\Delta t w_{j-1}^k, \mathbf{L}[k] + d_j\Delta t \phi_{j-1}^k)$

$\phi_j^k \leftarrow f_4(\mathbf{t}[k] + c_j\Delta t, \mathbf{V}[k] + d_j\Delta t m_{j-1}^k, \mathbf{A}[k] + d_j\Delta t w_{j-1}^k)$

▷ c_j and d_j are: $d_1 = c_1 = 0$, $d_2 = d_3 = c_2 = c_3 = 1/2$, $d_4 = c_4 = 1$.

9. Time-stepping loop $k = 1, \ldots, M+1$

(i) Evaluate age-integral for coupling in ODEs, i.e., $\int_0^{+\infty} s(a)i(a,t)da$

$I_k \leftarrow \mathsf{trapz}(s(a_j)\, i(a_j, t_{k-1}))$ ▷ Compute the *integral* term with the trapezoidal rule.

(ii) RK4 update of $\mathbf{T}$, $\mathbf{V}$, $\mathbf{A}$, $\mathbf{L}$

Compute $g_1^k, \ldots, g_4^k, m_1^k, \ldots, m_4^k, w_1^k, \ldots, w_4^k, \phi_1^k, \ldots, \phi_4^k$

$\mathbf{T}[k] \leftarrow \mathbf{T}[k-1] + \frac{\Delta t}{6}(g_1^{k-1} + 2g_2^{k-1} + 2g_3^{k-1} + g_4^{k-1})$

$\mathbf{V}[k] \leftarrow \mathbf{V}[k-1] + \frac{\Delta t}{6}(m_1^{k-1} + 2m_2^{k-1} + 2m_3^{k-1} + m_4^{k-1})$

$\mathbf{A}[k] \leftarrow \mathbf{A}[k-1] + \frac{\Delta t}{6}(w_1^{k-1} + 2w_2^{k-1} + 2w_3^{k-1} + w_4^{k-1})$

$\mathbf{L}[k] \leftarrow \mathbf{L}[k-1] + \frac{\Delta t}{6}(\phi_1^{k-1} + 2\phi_2^{k-1} + 2\phi_3^{k-1} + \phi_4^{k-1})$

(iii) Crank–Nicolson update of i_j^k *to approximate* $i(a_j, t^k)$

Build the vector $\mathbf{u} \in \mathbb{R}^N$ with the entries $\zeta \mathrm{i}_{j-1}^k + \left(1 - \frac{\Delta t}{2} s(a_j)\right)\mathrm{i}_j^k - \zeta \mathrm{i}_{j+1}^k$

Solve the system: $\mathtt{M}_{\mathrm{CN}}\mathbf{i}^k = \mathbf{u}$ ▷ Eq (3.5)

Store $\mathbf{M}[k, 1{:}N] \leftarrow \mathbf{i}^k$

Enforce the first column of $\mathbf{M}$ as $\mathbf{M}[k, 0] \leftarrow \lambda\, \mathbf{T}[k]\, \mathbf{V}[k]$ ▷ $i(0,t) = \lambda\, T(t)\, V(t)$

10. Compute the absolute errors e_{abs} **at final time** t^{M+1} **(Eq** (3.12)**)**

▷ e_{abs} is to validate the numerical solution as $t \to \infty$ with the equilibrium point E^* or E^0.

(i) Calculate the equilibrium E^* *or* E^0*, depending on the value of* R_0

for $u_{num}^\star \in \{\mathbf{T}, \mathbf{V}, \mathbf{A}, \mathbf{L}\}$ **do** $e_{abs} \leftarrow |u_{num}^\star[t^{M+1}] - u_{exact}^\star|$

end for

$e_{abs,\mathrm{i}} \leftarrow |\mathrm{i}_j^{M+1} - i^*(a_j)|$

Print $\{e_T, e_V, e_A, e_L, e_{\mathrm{i}}\}$ ▷ Display the absolute errors corresponding to each variable.

11. Export the data file for plotting

for $Unum \in \{\mathbf{T}, \mathbf{V}, \mathbf{A}, \mathbf{L}, \mathbf{M}\}$ **do**

    write CSV file *Data_Unum_vs_t.csv* ▷ A file is generated for each model variable.

end for

Generate graphical representations of the model variables